Master's thesis

NTNU
Norwegian University of Science and Technology
Faculty of Information Technology and Electrical Engineering
Department of Electric Power Engineering

Sebastian Bruu Ringdal

Analysis of Demagnetization Faults in a Permanent Magnet Synchronous Machine utilizing the Stray Magnetic Field

Master's thesis in Energy and Environmental Engineering
Supervisor: Arne Nysveen
Co-supervisor: Hossein Ehya
June 2023

NTNU
Norwegian University of
Science and Technology

Sebastian Bruu Ringdal

Analysis of Demagnetization Faults in a Permanent Magnet Synchronous Machine utilizing the Stray Magnetic Field

Master's thesis in Energy and Environmental Engineering
Supervisor: Arne Nysveen
Co-supervisor: Hossein Ehya
June 2023

Norwegian University of Science and Technology
Faculty of Information Technology and Electrical Engineering
Department of Electric Power Engineering

NTNU
Norwegian University of
Science and Technology

Analysis of Demagnetization Faults in a Permanent Magnet Synchronous Machine utilizing the Stray Magnetic Field

Sebastian Bruu Ringdal
Norwegian University of Science and Technology
Department of Electric Power Engineering
Supervisor: Arne Nysveen
Co-supervisor: Hossein Ehya

***Abstract*—The permanent magnet synchronous machine (PMSM) is a high-performance device due to its high efficiency and high power to weight ratio. The machine is however prone to damages that can be detected by a sensor that is mounted in the stator frame to monitor the stray magnetic field. A finite element model of a PMSM Weg mode W22 is made to analyze the impact of different types of demagnetization faults like uniform-, one pole- and trailing edge demagnetization. This thesis focuses on the frequency spectrum differences between the healthy and the faulty scenarios between 50% load and full load. The analysis is conducted in Ansys Electronics Desktop.**

The frequency spectrums are gathered through the use of fast Fourier transform. For one pole demagnetization it was found that the odd harmonics following the series 1/3, 2/3, 4/3 and 5/3 times the fundamental frequency of 50 Hz, which are the subharmonics 16.67 Hz, 33.33 Hz, 66.67 Hz and 83.33 Hz had a percentage change of 75.5%, 86.5%, 87.9% and 83.5%. The rest of the subharmonics following the same pattern also had a large increase in amplitude dB. This pattern was also observed with 50% load. Trailing edge demagnetization of 1/8 of the magnet gave minor differences, but for 1/4 of the magnet a new subharmonic pattern appeared with following 1/4 divided by the pole pairs in the machine. This pattern was not observed with 50% load. The stray flux signal of the induced voltage in the sensor had a lower amplitude for the trailing edge scenarios than the healthy with a decrease of 2.6% for 1/8 magnet and 7.1% for 1/4 magnet from the peak value of healthy case.

For uniform demagnetization the amplitude of the frequency spectrum was reduced significantly for the subharmonics in full load but matching at half load. Analysing the stray flux signal directly of the induced voltage in the sensor had a large difference with spikes of an increase of 62.5% compared with healthy induced voltage for the uniform demagnetization.

The full load scenario was adjusted by applying all of the rated voltage in the q-axis and for 50% load the angle between the stator and rotor field was changed. This is done by applying voltage in the d-axis which is adjusted by an angle in the voltage derived by the Clarke and Park transformation.

***Index Terms*—Demagnetization, stray flux, frequency spectrum, trailing edge, uniform, fault detection**

I. Introduction

Electrical monitoring tools have been the subject of extensive research since the 1980s [1]. This is primarily due to the significance of these machines to the industrial sector, which is crucial to the economies of many industrialized countries [2] as they consume more than 50 % of the global electricity [3]. Permanent magnet synchronous machines (PMSMs) are becoming more and more common in high-performance operations when comparing to other types of AC machines. They can operate at higher speeds and have higher torque to current ratio, higher efficiency, and higher power to weight ratio than other AC machines [6]. They are increasingly being used in aircraft, electrical cars, robotic applications, nuclear power plants, submarines, medical and industrial servo drives. Some of these applications require continuous operation, making a PMSM drive breakdown unacceptable [7]. They have typically lower noise and are more robust, unfortunately they are still prone to faults and damages.

Early stage detection of faults and proper condition monitoring of the machine is required to be able to stop the machine going into further damage [8]. Some typical faults that can occur on the PMSM are mechanical faults like bearing damages and eccentricity, electromagnetic faults like demagnetization and short circuit in the stator winding.

The monitoring of the electromagnetic flux has become more prevalent due to improvements in sensor technology with smaller and less expensive sensors to track the flux and simplicity in the form that they can be placed outside on the stator frame to measure the stray magnetic flux. The number of electric motors with built-in flux sensors has increased and which can be utilized for fault diagnosis [9]. The stray magnetic field is primarily used for the detection of rotor position in permanent magnet synchronous machines, brushless dc motors and induction machines [10], [11]. By measuring the stray magnetic, the machine can continue running and does not need to be taken apart.

The market for PMSM is anticipated to increase at a compound annual growth rate (CAGR) of 10.33% from $20.73 billion in 2021 and is expected to reach $34.68 billion in 2026 [12]. The ongoing research on PMSMs around the world and the increasingly interest in PMSMs are motivational factors to ensure and prevent the machine from breakdown by using condition monitoring tools.

The objective of this master thesis is to analyze the impact of different types of demagnetization faults by calculating the stray magnetic field in healthy and faulty operation. In order to achieve the objective, analyses of the frequency spectrum acquired from numerical finite element simulations of a WEG mode W22 created by WEG, a Brazilian company have been conducted. The targeted faults are partial, trailing edge and uniform demagnetization. Different fault types in a permanent magnet synchronous machine have been derived to lay a foundation of the different fault types [14].

II. About the thesis

This master's thesis is a continuation of a specialization project TET4510, that was completed in the same subject of study in the fall of 2022. The report for the specialty project included a literature survey of different fault types that can occur in a permanent magnet synchronous machine and a few simulations results. The process of constructing the finite element simulation model is similar for both this thesis and the specialization project. However, the thesis goes in much more in detail and target different faults. The same software called Ansys Electronic Desktop are used. Here it is noted that when [13] is cited the section is an exact replication and when [14] is cited then it contains additional information or a 'modification' from the specialized project and contains similarities in accordance with novel principles against plagiarism from NTNU [15].

III. Theory

This section goes through the construction and a general understanding of PM machines relevant for this thesis. Further it explains the transformation from abc frame to dq frame, an understanding of harmonics, a proposed method to demonstrate the appearance of demagnetization harmonics and the Maxwell equations that is used in the FEM software.

A. PM construction

A permanent magnet synchronous machine (PMSM) is a synchronous electric machine where the rotor consists of permanent magnets (PMs). The machine is like any rotating electric machine consisting of a rotor and a stator where the stator is fixed and the rotor is rotating. Magnetic flux linkage between the stator and rotor causes the shaft to rotate. An essential feature that distinguishes the synchronous machine from other types of electric machines is the synchronous link between the rotating fields of the rotor and stator [48, p. 493]. This results in a fixed relationship between the frequency of the emfs and currents in the stator and the rotor speed given as

$$n_s = \frac{120 f_s}{2p} \tag{1}$$

where n_s is the synchronous speed of the rotor, f_s is the electrical supply frequency, p is the number of pole pairs.

The stationary stator sets up a time-varying magnetic field because of the alternating currents while the magnetic field from rotor is made by the permanent magnets ferromagnetic material. The airgap field is the field between in the air between the rotor and stator which is created through the interaction of these fields. Harmonics are explained later in the next chapter, III-C and the first harmonic of the air gap magnetic flux density can be expressed as

$$B_{m1} = \frac{2}{\pi} \int_{-0.5\alpha_i\pi}^{0.5\alpha_i\pi} B_m \cos\alpha d\alpha = \frac{4}{\pi} B_m \sin\frac{\alpha_i \pi}{2} \tag{2}$$

where α_i is the ratio of the average B_{avg}, to maximum value B_m of the normal component of the air gap magnetic flux density given as [58]

$$\alpha_i = \frac{B_{avg}}{B_m} \tag{3}$$

The electrical energy supplied by the stator windings is converted into rotational energy in the rotor shaft [14].

The flux density B is given by the magnetic field intensity H as

$$B = \mu_0 \mu_r H \tag{4}$$

for the flux path in the core and

$$B = \mu_0 H \tag{5}$$

for the flux path in air where $\mu_0 = 4\pi \cdot 10^{-7}$ H/m and μ_r in the range of 2000-35000 for ferromagnetic materials [16]. The flux ϕ over an area

$$\phi = \oint_s \vec{B} \cdot d\vec{s} \tag{6}$$

will be significantly larger in the magnetic core than in the air paths. A tiny amount known as the stray or external magnetic flux can leak into the stator frame and further into the surrounding air. Both the airgap field and the stray magnetic field can be measured and provide information regarding the health status of the machine [14].

The permanent magnets are ferromagnetic materials with high coercive force and are placed in the rotor. When it comes to the design of the PM, there are various options. The stator can either be outside or inside the rotor. The rotor design are divided into salient pole rotor where the quadrature inductance is not equal to the direct $L_q \neq L_d$ or non-salient pole rotor where the direct inductance is equal to the quadrature $L_d = L_q$. Some variations of the different types are visualised in Figure 1. Figure 1 e) and f) visualize layered rotors and Figure 1 c) and h) shows the rotor containing barriers as white rectangles.

The rotor is further divided into whether its a interior permanent magnet synchronous machine (IPMSM) Figure 1 a), where the magnets are inside the rotor or a surface

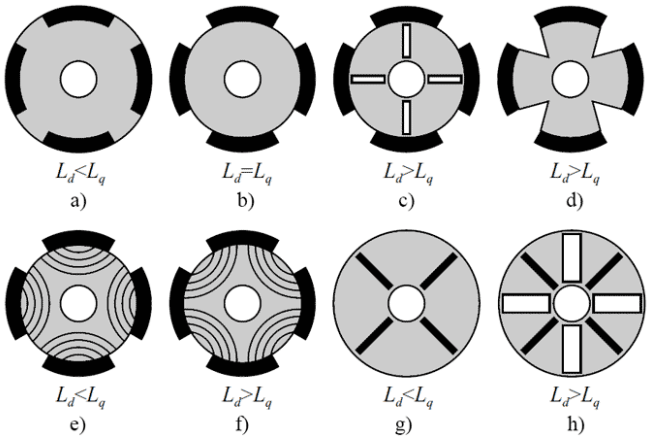

Fig. 1. The cross sections of PM rotors with different ratios of L_d/L_q, magnets in black [5]

permanent magnet synchronous machine (SPMSM) Figure 1 b), where the magnets are mounted on the surface of the rotor. The stator is consisting of a frame and a core with slots containing either two- or three-phase windings. The windings can be distributed in which the number of poles is not equal to the number of slots or concentrated where the number of poles is equal to the number of slots [14], [4].

B. abc to dq frame

In a later section of my thesis, I regulate the machine's torque using the dq frame, thus it is important to examine how the abc frame is changed into the dq frame. The Clarke transformation proposed by Edith Clarke, also known as the alpha-beta ($\alpha\beta$) transformation is a mathematical transformation from abc frame to the $\alpha\beta$ frame. The advantage of a $\alpha\beta$ transformation is that it can be used as a reference signal for space vector modulation control of three-phase inverters [22]. The Clarke transformation matrix is as following

$$K_c = \begin{bmatrix} 1 & -\frac{1}{2} & -\frac{1}{2} \\ 0 & \frac{\sqrt{3}}{2} & -\frac{\sqrt{3}}{2} \end{bmatrix} \tag{7}$$

In a balanced system the simplified transformation is done by multiplying the voltage-values with the Clarke matrix, [23] as following

$$\begin{bmatrix} v_\alpha \\ v_\beta \end{bmatrix} = \frac{2}{3} \begin{bmatrix} 1 & -\frac{1}{2} & -\frac{1}{2} \\ 0 & \frac{\sqrt{3}}{2} & -\frac{\sqrt{3}}{2} \end{bmatrix} \begin{bmatrix} v_a \\ v_b \\ v_c \end{bmatrix} \tag{8}$$

The Park transform is needed to transform from $\alpha\beta$ to the desired direct quadrature dq frame, proposed by Robert H. Park in 1929 [24]. The transform can rotate a vector's reference frame at a arbitrary frequency. The Park transform changes the frequency spectrum of the signal so that the arbitrary frequency is now represented as "dc," and the previous dc is now represented as the negative of the arbitrary frequency. The Park transformation matrix is as following

$$K_p = \begin{bmatrix} \cos(\theta(t)) & \sin(\theta(t)) \\ -\sin(\theta(t)) & \cos(\theta(t)) \end{bmatrix} \tag{9}$$

where $\theta(t) = \omega t + \theta_0$ is rotating with the angular speed of the rotor ω. θ_0 corresponds to the initial angle between the α-axis and the d-axis as shown in Figure 2.

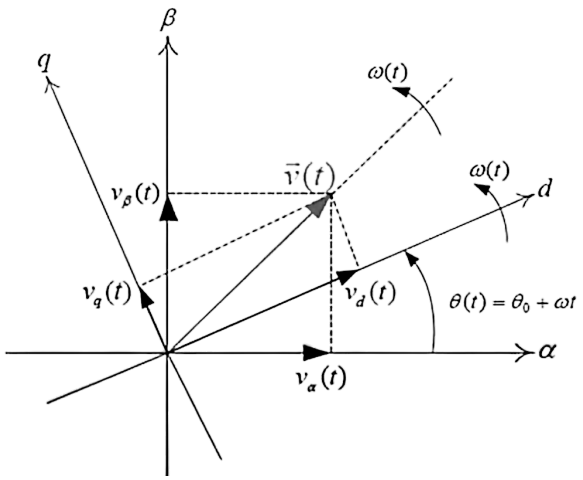

Fig. 2. $\alpha\beta$ frame and dq frame [21]

Further the voltage values for $\alpha\beta$ frame are multiplied with the Park matrix

$$\begin{bmatrix} v_d \\ v_q \end{bmatrix} = \begin{bmatrix} \cos(\theta(t)) & \sin(\theta(t)) \\ -\sin(\theta(t)) & \cos(\theta(t)) \end{bmatrix} \begin{bmatrix} v_\alpha \\ v_\beta \end{bmatrix} \tag{10}$$

The process of transformation can be summarized in one equation as

$$v_{dq}(t) = K_c K_p v_{abc}(t) = K_{cp} v_{abc} \tag{11}$$

where K_{cp} is the combination matrix of the $\alpha\beta$ and the dq frame. The equation 11 can be expressed as a matrix equation where the dq frame is expressed with the abc values.

$$\begin{bmatrix} v_d \\ v_q \end{bmatrix} = \begin{bmatrix} \cos(\omega t+\theta_0) & \cos(\omega t-\frac{2\pi}{3}+\theta_0) & \cos(\omega t+\frac{2\pi}{3}+\theta_0) \\ -\sin(\omega t+\theta_0) & -\sin(\omega t-\frac{2\pi}{3}+\theta_0) & -\sin(\omega t+\frac{2\pi}{3}+\theta_0) \end{bmatrix} \begin{bmatrix} v_a \\ v_b \\ v_c \end{bmatrix} \tag{12}$$

C. Harmonics

Harmonics are sinusoidal oscillations at frequencies that are multiples of the fundamental frequency. The fast Fourier transform can show which harmonics that are present as described in the previous section V-B. The fundamental frequency has the same frequency as the power supply frequency. In a frequency spectrum the fundamental frequency can be found as the spike with the largest amplitude. The 2nd harmonic is the frequency in which has the double the frequency of the fundamental, the 3rd harmonic is the frequency wave having three times the fundamental frequency and so on.

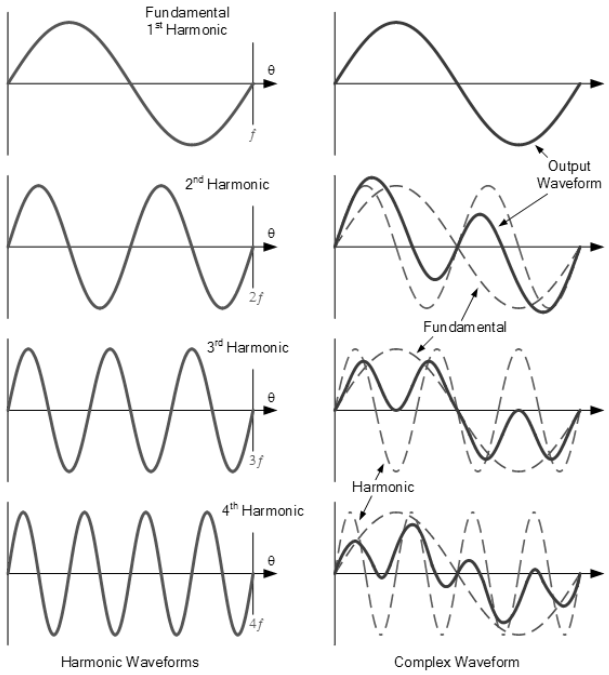

Fig. 3. Harmonics visualized in waveform [51]

In Figure 3, it is shown how harmonics are added together and make up a complex waveform. Odd harmonics are symmetric about the x-axis while even harmonics are unsymmetrical. The voltage is symmetrical due to the symmetry of the field system and the coils, so the even harmonics are typically absent or damped [14], [32]. It is possible to alter the values of inductance and capacitance to get resonance at the fundamental frequency. Several methods to minimize or eliminate the harmonic components like injecting current waveform [46], increase the length of the airgap to increase the reluctance and using a PI controller [47].

D. Demagnetization

In [34] there has been a proposed method to demonstrate the appearance of new harmonics generated by the demagnetization fault for a PMSM which is described in this section. The permanent magnets placed in the rotor generate a back electromotive force (EMF) in the stator windings. In a healthy case with normal operation the back EMF voltage in each slot of the stator windings is periodic and consistent. However, if there is a demagnetization fault such as partially demagnetized magnets, the back EMF induced in a single slot will be lower than normal. This can result in a asymmetry in the waveform whenever a demagnetized magnet moves in over the analyzed slot. The back EMF in a single slot is halved when a pole is 50% demagnetized, as shown in Figure 4.

This is modelled by subtracting the waveform $g(t)$ from the sinusoidal waveform $e(t)$ illustrated in Figure 4. The wave $g(t)$ which is a normalized voltage drop can be derived mathematically by multiplying the fundamental sinusoidal wave with a rectangular wave $r(t)$ given as a Fourier series:

$$r(t) = \frac{1}{2p} + \sum_{k=1}^{\infty} \frac{2}{k\pi} \sin(\pi k d) \cos\left(\frac{2k\pi f_e t}{p}\right) \tag{13}$$

which has a frequency of f_e/p and a duty cycle of $d = 1/2p$.

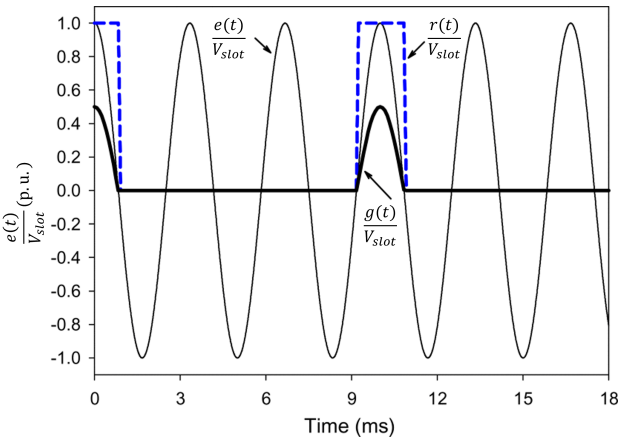

Fig. 4. Waveforms that are used for modeling effect of demagnetization on the back EMF [34]

The multiplication as explained yields

$$g(t) = \cos(2pf_e t)\left[\frac{1}{2p} + \sum_{k=1}^{\infty} \frac{2}{k\pi} \sin(\pi k d) \cos\left(\frac{2k\pi f_e t}{p}\right)\right] \tag{14}$$

where the equation 14 can further be simplified to

$$g(t) = \frac{1}{2p}\cos(2\pi f_e t) + \sum_{k=1}^{\infty} \frac{1}{k\pi} \sin\left(\frac{k\pi}{2p}\right) \cos\left[2\pi f_e t\left(1 \pm \frac{k}{p}\right)\right] \tag{15}$$

As a result, the induced voltage in the first slot of phase a can be described as:

$$\frac{d\lambda_{slot}(t)}{dt} = V_{slot}\cos(2\pi f_e t) - V_{slot}K_{dem}g(t) \tag{16}$$

where K_{dem} is the percentage of the demagnetization and V_{slot} is the amplitude of the back EMF in a single slot. The induced back EMF e_1 in the first slot of phase a can be now be expressed by substituting 15 into 16.

$$e_1(t) = \frac{d\lambda_{slot}(t)}{dt} = V_{slot}\left(1 - \frac{K_{dem}}{2p}\right)\cos(2\pi f_e t) - V_{slot}K_{dem}\sum_{k=1}^{\infty} \frac{1}{k\pi} \sin\left(\frac{k\pi}{2p}\right) \cos\left[2\pi f_e t\left(1 \pm \frac{k}{p}\right)\right] \tag{17}$$

The back EMF is reduced by a factor $(1 - \frac{K_{dem}}{2p})$ and the other part $(1 \pm \frac{k}{P})$ is seen in literature [59] - [61], as a following set of harmonics frequencies were induced in the stator current spectrum by the demagnetization

$$f_{demag} = f_s(1 \pm \frac{k}{P}) \tag{18}$$

f_s is the electrical supply frequency, k is an integer and P is the number of poles. The same frequency harmonics that are present in the stator current should also be present in stray magnetic flux.

E. Maxwell Equations

The Maxwell equations are the foundation for describing all electromagnetic interactions and they are used in Ansys Maxwell. The following equations, along with the Lorentz force and motion equations, describe all electromagnetic conversions relevant to rotation machinery [62]. Amperes law introduces displacement current, a source of the magnetic field, in parallel with the ordinary current:

$$\boldsymbol{\nabla} \times \mathbf{H} = \mathbf{J} + \frac{\partial \mathbf{D}}{\partial t} \tag{19}$$

where H is the magnetic field strength, J is the total electric current density, D is the displacement field.

The magnetic flux flows in closed loops which is described by the equation:

$$\nabla \cdot \mathbf{B} = 0 \tag{20}$$

where B is the magnetic field. According to the electric field's Gauss law, charges cause an electric field to flow from the source with a new return path as follows:

$$\nabla \cdot \mathbf{D} = \rho \tag{21}$$

where ρ is the total electric charge density. In Amperes law, the displacement current is introduced in parallel with the regular current and serves as a source for the magnetic field:

$$\boldsymbol{\nabla} \times \mathbf{E} = -\frac{\partial \mathbf{B}}{\partial t} \tag{22}$$

where E is the electric field.

IV. Faults in PMSMs

In this section there are explained some of the different type of faults that can occur in a permanent magnet synchronous machine.

A. Inter turn short-circuit

One of the most major faults that can occur in the PMSM is inter turn short circuit (ITSC), which can be difficult to identify but can result in significant damage [49], [50]. The types of the short circuit faults can be classified into inter turn fault, inter phase fault and phase to ground fault. The fault often start as a turn to turn fault and develop into an inter phase fault or a phase to ground fault [13], [52].

Insulation degradation, which can be brought on by heat stress, mechanical stress, moisture and partial discharge, between the windings in the same phase is usually the cause of the ITSC. Shorted turns form a loop connected to the original winding after the initial fault. The back-EMF and inductor coupling serve now as voltage sources. The circulating fault current is the opposite phase of the input current, generating a reverse magnetic flux opposing the main flux, though serving as current limiters [53]. The circulating current can be significantly greater than the rated current and the shorted turns' impedance is low, both of which can raise the thermal stress on the damaged windings. This may cause surrounding turns to be affected by faulty windings, which may eventually cause phase to phase or phase to ground fault [54]. Although the insulation failure is more likely to result in a phase to ground than a phase to phase fault, the inter turn fault may not be detected before it has turned into a ground fault. As mentioned in section demagnetization inter turn short circuit can lead to partial demagnetization. This can happen because of the huge eddy current leading to a overheating of the motor beyond the Curie point [13], [55].

A healthy PMSM maintains the symmetry of the stator windings with balanced stator currents generated via a three phase power supply connection. However, when an inter turn short circuit occurs, it leads to a reduced ampere-turns in the affected pole resulting in a weakening of the MMF and magnetic field generated by that pole. The stator windings and the airgap field become asymmetric and the three phase stator current amplitudes are then no longer balanced. The asymmetric airgap field can distort the force distribution which can lead to unbalanced magnetic pull (UMP). UMP can cause mechanical stress on the winding insulation and increasingly vibration level. The thermal stresses also increase and the overall temperature of the machine can be higher than normal which can lead to a degradation of the performance and efficiency of the machine [13].

B. Eccentricity

Eccentricity fault is defined as as the nonuniform airgap distribution between stator and rotor due to displacement of the stator or rotor symmetrical axis. The displacement can either be static, dynamic or a combination of both. Static eccentricity (SE) is when the rotor symmetrical and rotational axis is displaced from the stator symmetrical axis. The airgap will then be shorter on one side compared with the other side. Dynamic eccentricity (DE) is when the rotor symmetrical

axis is displaced from the stator symmetrical axis but the rotor rotational axis is the same as the stator symmetrical axis. Mixed eccentricity is when a combination of DE and SE faults occur. Dynamic and static eccentricity are shown in Figure 5 [14], [17].

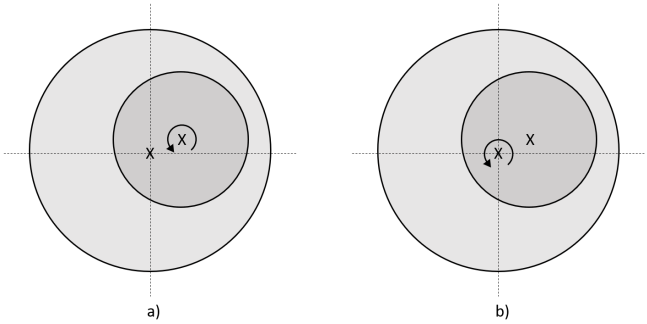

Fig. 5. a) Static eccentricity, b) Dynamic eccentricity

Eccentricity can cause an unbalanced magnetic pull (UMP) where the airgap is the smallest and can lead to mechanical stress on the shaft and bearings [1], [56]. If this goes on for a while, the rotor may finally scrape against the stator core's surface and cause serious damage to the PMSM. The PMSM can be optimized in the machine design in order to reduce the UMP [57], [14].

C. Demagnetization

The magnets in a PMSM are prone to damage and faults such as demagnetization which can result in a performance degradation of the motor. The ferromagnetic material that makes up magnets surrounds itself with a magnetic field. This field can be weakened, and is then referred to as demagnetization. A combination of mechanical, electrical, thermal, ambient operating stress such as significant temperature raise, cracks in the magnet, inter turn short circuits or high stator currents are the main contributing factor to irreversible demagnetization. [18]–[20].

1) Partial demagnetization: An armature reaction caused by a situation where a strong torque is needed can cause demagnetization. The electrical current of the stator winding creates an inverse magnetic field during the normal operation of the PMSM, which opposes the remanent induction of the permanent magnets. Therefore, the demagnetizing will take place because of the change of the orientation of the magnetic dipoles. This phenomenon happening multiple times causes demagnetization in the permanent magnets. This demagnetization can be complete, meaning it affects the entire pole, or partial, meaning it affects only a portion of the pole. [26]

A turn-to-turn short circuit fault can partial demagnetization a surface mounted magnet. The worst case condition is when the motor is operating at a high load and a whole coil is short circuited [28]. Then, the armature reaction is at its highest point and will affect the permanent magnets. Some permanent magnet like NdFeB corrode or cracks formed during he manufacturing process can lead to disintegration at high speeds which again can cause flux disturbances [30].

The stator currents during a partial demagnetization are higher than they would be in a healthy PMSM running under the same load conditions. As a result, the PMSM's thermal level rises [25]. From the perspective of mechanical performance, partial demagnetization result in an unbalanced magnetic pull. Due to the magnetic force harmonics produced by this phenomenon, the machine becomes noisy and vibrates [28].

2) Uniform demagnetization: In the automotive industry, a compact motor design with high winding fill factor and a strong magnetic field in the permanent magnets are required. This can cause troubles with cooling the machine [42]. High temperature increased past the Curie point alter the magnetic dipoles which will be freed from their ordered alignment by the energy. By repeatedly striking a magnet or applying pressure the same result can be achieved. The physical disturbance and vibration, which knock the order out of it [27].

High-temperature and overload working environment and PM material age limitations can cause uniform demagnetization because all of the magnets are affected. As with partial demagnetization the input current of the motor has to be increased to maintain the same torque output capacity after the demagnetization fault. This is because the no-load back EMF of the motor has been decrease which cause a smaller output capacity and affect the performance of the motor [35]. Diagnosing uniform demagnetization is more difficult than partial demagnetization due to that there are no asymmetry.

3) Trailing edge demagnetization: The magnets in a PMSM have one leading edge and one trailing edge. The leading is the rotation direction followed by the trailing edge which is behind. The magnetic axes of the stator MMF and the PM are not aligned during an operation where the stator current vector is ahead of the q-axis. This is illustrated in Figure 6.

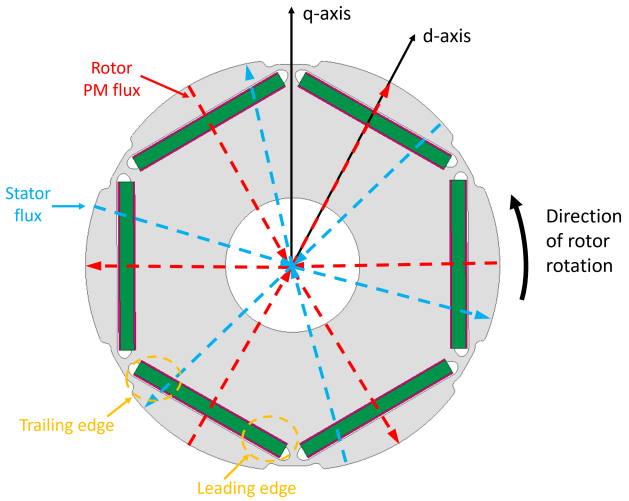

Fig. 6. Stator flux affecting the trailing edge of the magnets

As a result, the stator's MMF output is focused near the

permanent magnet's trailing edge and is likely to lead to demagnetization in the trailing edge of all the magnets in the PMSM [31]. In [33], it is showed that the only technique that can reliably identify trailing edge demagnetization and separate it from other fault types is airgap flux-based monitoring, while in this thesis the stray magnetic field is used.

V. Condition Monitoring

In this section, the theory behind how the magnetic flux can be utilized in condition monitoring of electrical machines. Further how signal processing tools with the focus of fast Fourier transform are used to analyze the magnetic flux as it is used in this thesis.

Numerous methods for monitoring electrical machinery have been developed over time. To find the defect, many physical quantities can be measured, including magnetic flux, temperature, acoustic noise, stator and rotor current, and mechanical vibration. Each one has advantages and disadvantages and each specific technique is constrained by specific limitations. As a result, no approach exists to identify every malfunction that frequently arises in an electric rotating machine [36]. This has lead to a large number of research that concentrate on the evaluation of various electrical machine signals in order to identify the best option. Due to a variety of advantages and benefits above earlier traditional methods, studying the magnetic flux has caught the attention of many researchers [14].

A. Magnetic flux

The most common way to analyze the magnetic flux is by analyzing the airgap flux. The airgap flux is located between the rotor and the stator. Analyzing the external flux also known as the stray flux, which leaks outside the machine frame, can also be done. The axial stray fluxes at the end of the machine are primarily caused by end-winding currents and permanent magnet leakage fluxes, while the radial stray fluxes are caused by end-winding leakage fluxes [37]. The axial and radial directions are visualised in Figure 7. The flux density of stray flux is often quite low for machines with steel frames and decreases with distance from the machine's surface. Although minimum leakage flux are desired for the best electrical machine functioning and design, the leakage flux can provide information of the health of the electrical machine. The external flux is typically 10^{-4} to 10^{-5} times lower than the airgap flux but they have the same shape [8]. Some selection parameters that need to be considered are size, resolution, frequency range, sensitivity, and cost. Sensitive sensors are needed to capture weak stray fluxes for external measurements [37].

Some different type of flux sensors with different advantages and disadvantages are Hall-effect flux sensors (HEFSs), magnetostrictive (MS) materials, magnetoresistors (MRs), flux-gate magnetometers (FGMs) and search coils (SCs). As search coils are the ones that are used in this thesis and they are explained further. When exposed to an external magnetic

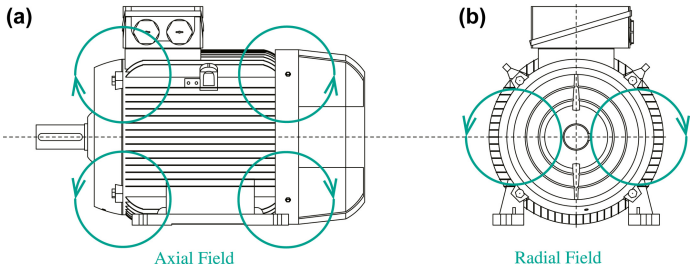

Fig. 7. Major flux directions, a) showing the axial field, b) showing the radial field [37]

field, they will produce voltage according with the formula for induced voltage e

$$e = N\frac{d\phi}{dt} = NA\frac{dB}{dt} \tag{23}$$

where N is the number of turns, ϕ is the flux, B is the airgap flux and A is the surface area enclosed by the coil. The coils can be made by hand or by a manufacturer, and they come in different shapes like rectangular, circular, and C-shaped [38]. It could be significant noise in the SCs which can be explained by the derivative in the equation (23). Additionally, SCs are less sensitive than other sensors like HEFSs since the flux is only indirectly monitored in SCs [37]. Figure 8 shows how the some of the different flux sensors can be placed in to analyze the flux in an electric machine [14].

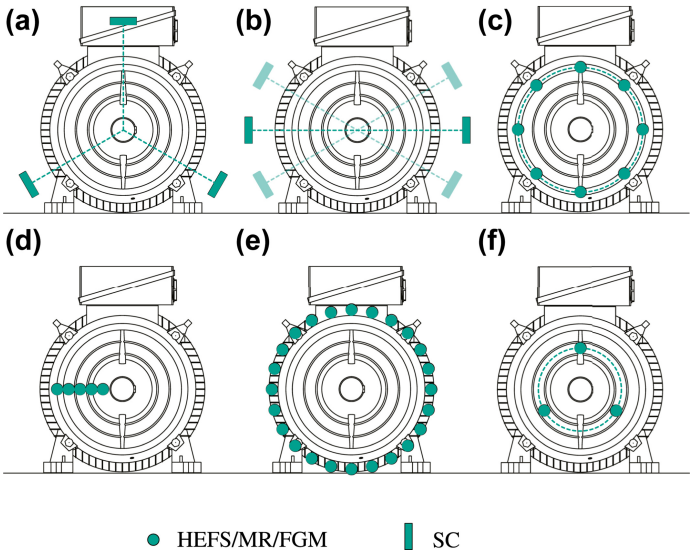

Fig. 8. Different settings for placements of external flux sensors [37]

Several advantages have proven exist for the analysis of the magnetic flux like very low cost sensors and simplicity and flexibility of the installation, not a previous knowledge of the healthy operation, efficient and reliable the cases where previously methods have caused false indications [39]–[41]. For the analyzing of the stray flux, it is a noninvasive method that can save the effort of disassembling the machine, and therefore is an emerging trend in the recent years. Although

there are many advantages there are some disadvantages worth noticing like the influence of the sensor position affecting the results, taking apart the machine to install sensors in the airgap, the need of expert knowledge to analyze the data, similar patterns for DE and ITSC fault and difficulties arising when modelling faults in specific parts of the motor due to asymmetry during faults [8], [14], [41], [42].

B. Signal processing

An essential component of condition monitoring is signal processing which lays the groundwork for accurate analysis. A signal's amplitude, period, or variance are examples of time domain characteristics that can be exploited to provide information about the signal source. The frequency spectrum is however more commonly used in condition monitoring of electrical machines. To convert time domain data into a frequency domain representation, a variety of processing techniques can be used.

Fourier transform and especially the fast Fourier transform (FFT) is one of the most used techniques to transform the signal from the time domain to the frequency domain. This technique works well for examining the many harmonics in a fault signal. To obtain sufficient frequency precision, the Fourier transform must be calculated over a significant amount of time [43, p 489]. The FFT is an algorithm that calculates the discrete Fourier transform (DFT) of a sequence. The formula

$$X_k = \sum_{n=0}^{N-1} x_n e^{-i2\pi kn/N} \tag{24}$$

defines the DFT for $k = 0, ..., N-1$, where $e^{-i2\pi kn/N}$ is an N-th primitive root of unity, X_k is a sequence of complex numbers and x_n is a sequence of samples. DFT is using a fixed sampling interval to record a discrete time signal and covert it into the frequency domain. This is achieved by decomposing a sequence of values into components with various frequencies [44]. The FFT is factorizing the DFT matrix into a result with factors of mostly zeros, thus reducing the complexity from $O(N^2)$ to $O(NlogN)$, where N is the data quantity [14], [45].

To calculate the spectrum of either a continuous time or discrete time signal, the signal's values for all time are required. However, in practice, we only monitor signals for a limited amount of time and therefore only an approximation of the spectrum may be obtained from a limited data record. Further, by using the DFT one can analyze an analog signal that passes through an anti-aliasing filter with a rate of $F_s \geq 2B$. B is the bandwidth of the filtered and $F_s/2$ is the highest frequency that the sampled signal contains. The duration of the signal can be limited to $T_0 = LT$, where T is the sample interval and L is the number of samples. The finite observation interval limits our ability to distinguish two frequency components that are separated by less than $1/T_0$.

The sequence to be analyzed is $\{x(n)\}$ and the duration of the interval to $0 \leq n \leq L-1$
which is equal to multiply $\{x(n)\}$ by $\omega(n)$ a rectangular window with the length L following the equation

$$\hat{x}(n) = x(n)\omega(n) \tag{25}$$

where $\omega(n)$ is

$$\omega(n) = \begin{cases} 1, & 0 \leq n \leq L-1 \\ 0, & \text{otherwise} \end{cases} \tag{26}$$

If the sequence $x(n)$ consist of a single and purely sinusoidal signal given as $x(n) = \cos \omega_0 n$, then the Fourier transform of the sequence can be expressed as

$$\hat{X}(\omega) = \frac{1}{2}[W(\omega - \omega_0) + W(\omega + \omega_0)] \tag{27}$$

where

$$W(\omega) = \frac{\sin(\omega L/2)}{\sin(\omega/2)} e^{-j\omega(L-1)/2} \tag{28}$$

which is the Fourier transform of the window sequence of the rectangular window [43, p 489].

By using DFT the sequence $\hat{x}(n)$ can be padded with N-L zeros and the N-point of the truncated L points sequence can be computed. The magnitude spectrum of $|\hat{X}(\omega)|$ is placed in Figure 9 with $N = 1024$, $L = 31$ and $\omega = 2\pi 100$.

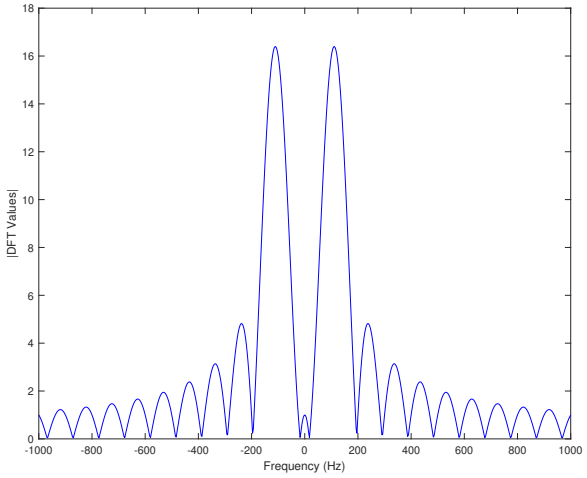

Fig. 9. Magnitude spectrum for L=31 and N=2048, illustrating the occurrence of leakage

It is evident that the windowed spectrum is dispersed across the entire frequency range rather than being localized to a single frequency which is a feature of windowing the signal known as leakage. This issue can be resolved by multiplying the signal with a window function with lower side lobes in the frequency domain. However, a decrease in the side lobes results in an increase in the main lobe, which results in a loss in the resolution [43, p 491].

VI. Modelling and simulation

This chapter contains information about the PMSM, the simulation setup and the modelling techniques used in the FEM software.

The analysis was conducted by using the FEM software Ansys Electronic Desktop where the module Maxwell is used. The permanent magnet synchronous machine W22 Weg Mode is implemented in Ansys which is used to break an area into a finite number of smaller components, analyze each component, and then put the components back together to show the result in the original setup. The origin and design of the machine is explained, the relevant properties, materials and nominal data is placed in this section. The design data of the machine is placed in Appendix C in Table III.

The complex modeling places a tremendous demand on the CPU, necessitating the usage of a remote desktop connection to perform the simulation faster. The simulations are run on two local servers at NTNU where one simulation takes about 24 hours.

A. PMSM parameter specifications

The machine is produced by WEG which is a Brazilian company that operates worldwide in electrical engineering, power and automation technology. The parameters for the W22 Weg Mode PMSM is placed in Table I. The IPMSM Maxwell model of the machine is based the physical model WEG W22. Figure 10 illustrates the stator windings in the motor, which are single-layered, bifurcated, and distributed with integer windings with coil ends of three levels. The materials are not given so they are estimated. The physical WEG W22 is delta-coupled which is changed to star-connected for the Maxwell model so the base value of the voltage is $1/\sqrt{3}$ of whats given on the nameplate [29].

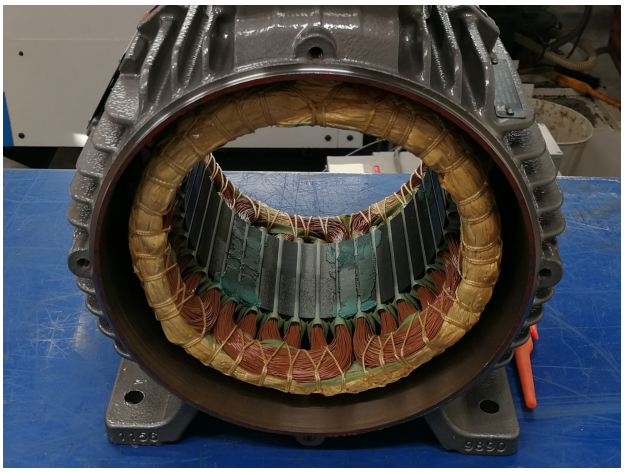

Fig. 10. Stator of the physical motor WEG W22 [29]

B. Materials

1) Steel: The Maxwell library's steel1010 material were applied to the rotor and stator steel and the red part outside the magnets. The BH-curved for the steel is shown in Figure 11.

TABLE I
PMSM nominal data

Voltage	$\sqrt{2}/\sqrt{3} \cdot 400$ V
Speed	1000 rpm
Frequency	50 Hz
Pole pairs	3

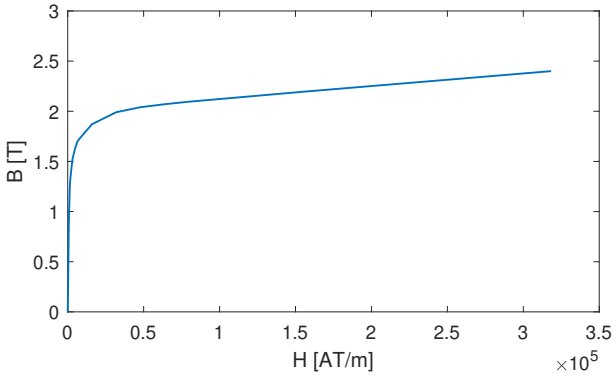

Fig. 11. The BH-curve of core material

The bulk conductivity is $2 \cdot 10^6$ S/m and the mass density is 7872 kg/m^3.

2) Permanent magnets: For the permanent magnets the material called XG196/96_2DSF1.000 were chosen with the BH-curve in Figure 12.

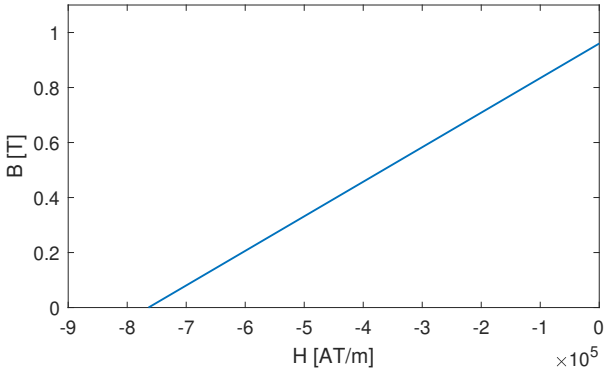

Fig. 12. The BH-curve of a healthy PM

The conductivity is 0 S/m, which means the magnets will not conduct any current. The coercivity is 763944 A/m and the remanence is 0.96 T.

3) Coils: Maxwell library of the material called "copper" is chosen. It has relative permeability of 0.999991, bulk conductivity of $5.8 \cdot 10^7$ S/m and mass density of 8933 kg/m^3. The coils have air that surrounds them which has relative permeability of 1.0000004 and mass density of 1.1614 kg/m^3.

C. Rotor

The rotor consists of 3 pole pairs which is made up by 6 interior mounted permanent magnets. Real rotors contain thin lamentations to reduce eddy currents, which is not the case in this model. Steel and permanent magnet material properties explained in the previous section were applied respectively to the rotor steel and the magnets. The shafts material is chosen as air and is not taken into consideration because it has little impact on the simulation [14].

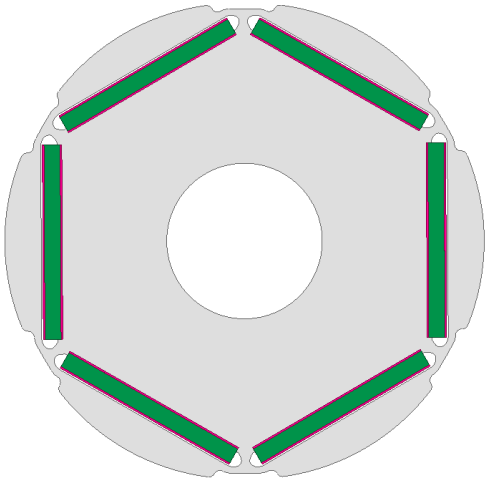

Fig. 13. Rotor of the Maxwell IPMSM model.

D. Stator

The stator is made up of 36 slots, stator yoke and stator teeth in between the slots [14]. The slots are single-layered following the pattern visualized in Appendix A. The steel is the same as for the rotor. The stator core is solid as the core losses are neglected and surrounded by air. A sensor is mounted on top of the stator frame to detect the stray magnetic flux with the chosen material copper and with 1000 turns.

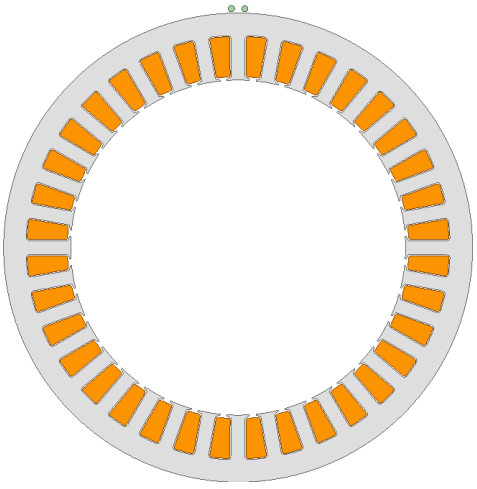

Fig. 14. Stator and sensor of the Maxwell IPMSM model.

E. Mesh

The model's breakdown into finite elements is described by the mesh. Each node at the intersections of neighboring elements are solved numerically for each time step of a simulation and the area inside the elements is solved by interpolation. In order to achieve a sufficient level of simulation accuracy while keeping the calculation time reasonable, the size of the model's elements had to be specified. The air gap is a critical area where accurate calculation of the flux density is important and therefore has been given a more dense mesh than the rest of the machine. The mesh for the stator has also been defined to be finer as the stray flux that is analyzed outside the stator frame moves through the stator yoke.

A mesh technique called inside selection is used to create the desired resolution in the different parts of the PMSM. As seen in Figure 15, the airgap has a more dense mesh in the zoomed section [14].

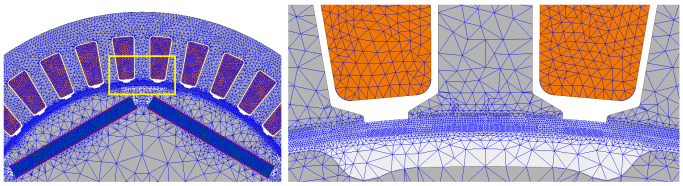

Fig. 15. Finite element mesh with a zoomed section showing the airgap

TABLE II
ELEMENT RESTRICTIONS

Object	Selection	Size restriction
Magnets and slots	Inside Selection	1 mm
Stator iron	Inside Selection	2 mm
Airgap	Inside Selection	0.2 mm

F. Analysis setup

Important parameters that affect the accuracy of the results as well as the computational time and resources are determined by the solution setup. One mechanical revolution of the PMSM takes 60 ms. Eight revolutions is preferable to have precise calculation of the frequency components and a high frequency resolutions of the FFT, therefore the total simulation is corresponds to 480 ms. Although, this was changed to 3 s due to that the resolution of the FFT was not high enough which was found throughout the testing process. The sampling frequency is set to 10 kHz with a time step of 0.1 ms. All simulations made use of the transient solver which calculates the time-varying magnetic field at each time step. The time integration method used is backward Euler and fields are saved every 100 ms. The expression cache is used to calculate the airgap flux at each time step. The nonlinear residual is set to 0.01 ms.

G. Airgap flux

The method for calculating the airgap flux is done by setting a calculation for the radial B-field in the Calculator inside Maxwell and assigned it to a point as showed in Figure 16. The expression cache data can further be plotted through a Transient report in the Analysis settings in Maxwell.

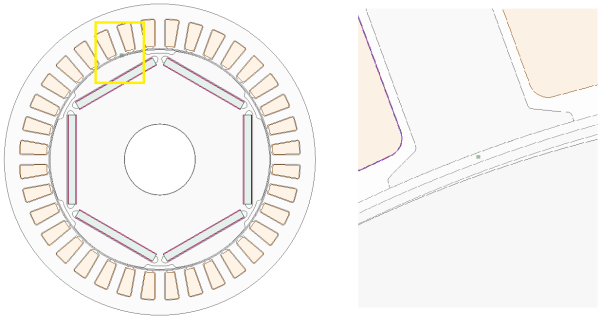

Fig. 16. Location of airgap point

H. Full load and 50% load

The full load is applied when the voltages are applied to the different phases with the following equations:

$$V_a = V_p * \cos\left(2\pi\omega t + \frac{2\pi}{3} + \theta\right) \tag{29}$$

$$V_b = V_p * \cos\left(2\pi\omega t - \frac{2\pi}{3} + \theta\right) \tag{30}$$

$$V_c = V_p * \cos\left(2\pi\omega t + \theta\right) \tag{31}$$

where V_p is $400\frac{\sqrt{2}}{\sqrt{3}}$ and the angle θ to align the voltage with the q-axis is $\theta = 2\pi f t_{max}$. This angle θ is found through a time dependent study where the excitation is changed to current and set to zero to observe the magnetic field from the magnets. The time with the maximum torque gives the t_{max} in θ which was found to be 1.1 ms, see Figure 38 in Appendix B. A simulation for both healthy and faulty is obtained. For 50% loading condition, the angle θ is adjusted to 0.05 ms so that more current will flow in the d-axis which gives less torque. This is the same θ_0 in equation 12 in section III-B. The angle between the stator and rotor field is changed and therefore the torque also changed.

I. Demagnetization

The permanent magnet (PM) demagnetization is the loss of the performances of the permanent magnets due to changes in the material. A linear BH curve is used to define the PM material properties. Figure 17 shows in blue the BH-curve for the healthy magnets and in red for the 50% demagnetized.

For the uniform demagnetization all of the magnets are 50% reduced. The trailing edge demagnetization is done by applying 50% demagnetization on the trailing edge of all the magnets with one case with the demagnetization covering 1/8 magnet and one with 1/4 of the magnet. For the one pole demagnetization case, two magnets that together make up one pole is demagnetized by 50%.

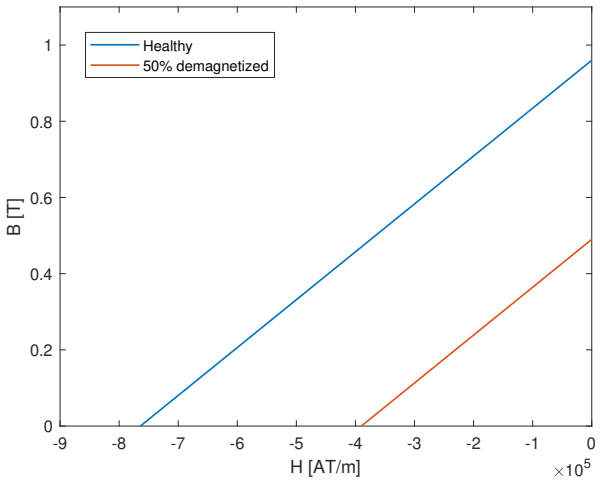

Fig. 17. The BH-curve of a healthy and faulty PM

VII. Simulation results and discussion

In this section the results are presented and discussed. It is not divided into two separate sections because by doing it this way it prevents the reader from having to jump back and forth between the results and discussion while reading.

A. Healthy

A 400V voltage is applied to all three phases in the full load scenario. Figure 18 shows the motor in a healthy case at full load at the start of the simulation.

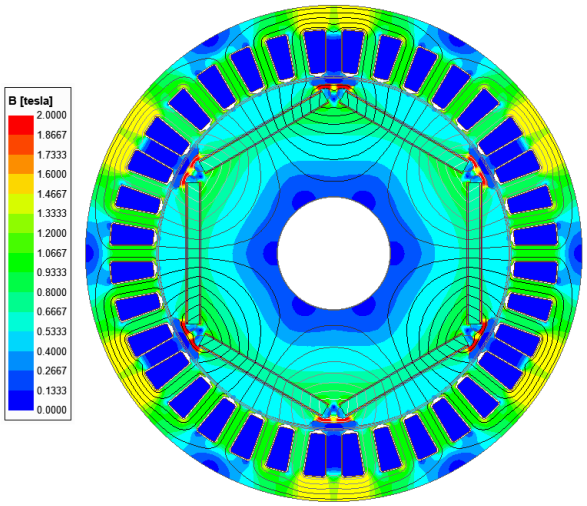

Fig. 18. Flux density of the full load healthy machine

Three periods can be seen as a result of the three pole pairs. Additionally, it is clear that the rotor field and stator field are perfectly synchronized. However, this different for the next time step as the stator field is a bit a head of the rotors field. The flux density in the teeth is at most 1 T, but the flux density peak in the yoke is closer to 1.4 T. A few red areas with a

value of approximately 2 T can be seen at the rotor's notches which is moving into saturated area following the BH-curve in Figure 11, [14].

The radial component of the magnetic flux density in the airgap for different full load and 50% load is given in Figure 19 for one full rotation of the rotor. The maximum about 1.1 T at full load and 0.86 T for 50 % load. This flux pattern is repeated for every rotation.

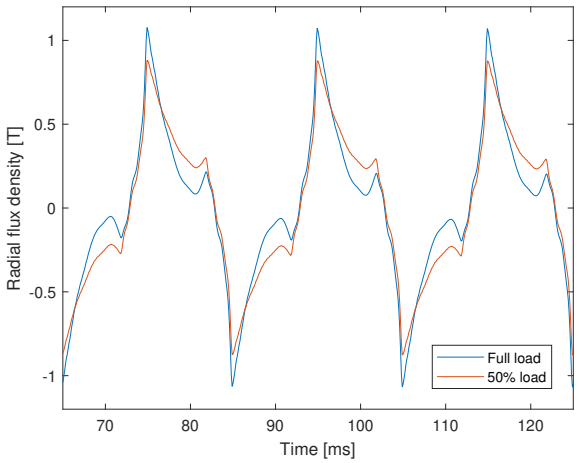

Fig. 19. Healthy case, Radial airgap flux densities

The tangent component of the magnetic flux density in the airgap is given in Figure 20 for both full and 50% load with respectively maximum values of 0.05 T and 0.037 T.

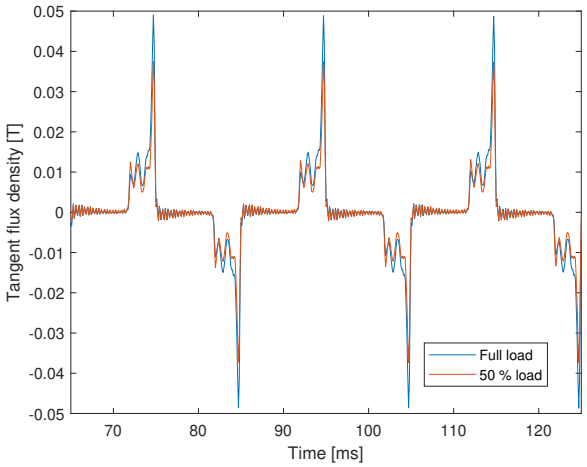

Fig. 20. Healthy case, Tangent airgap flux densities

Figure 21 shows the magnetic flux density of the stray flux in a vector form. The flux radiates outside the stator yoke and follow the same direction as the magnetic field that radiates inside the machine which can be seen by the direction the vectors are pointing. The strength of the magnetic field is in the interval $[0, 0.003]$T. The average magnetic flux density outside of the machine is about 0.15% of the average magnetic flux density inside the machine.

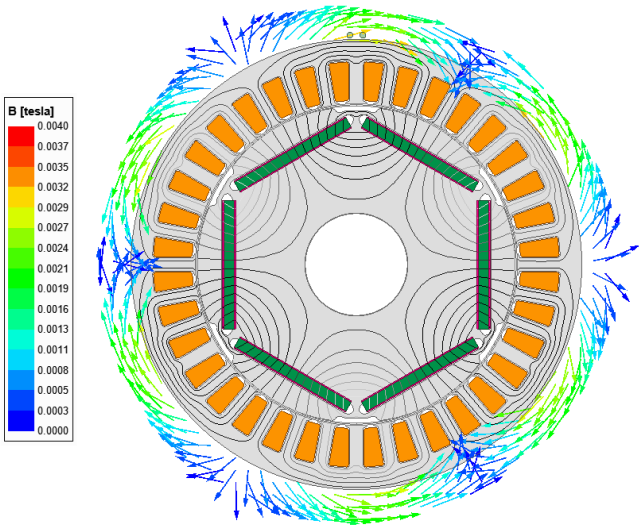

Fig. 21. Flux density of the stray flux in a full load healthy machine

The FFT of the stray flux is placed in Figure 22. The frequency with the highest amplitude is the fundamental frequency of 50 Hz. The odd harmonics of 150 Hz, 250 Hz, 350 Hz, etc have higher amplitudes than the even harmonics of 100 Hz, 200 Hz, 300 Hz which is expected and explained in subsection III-C.

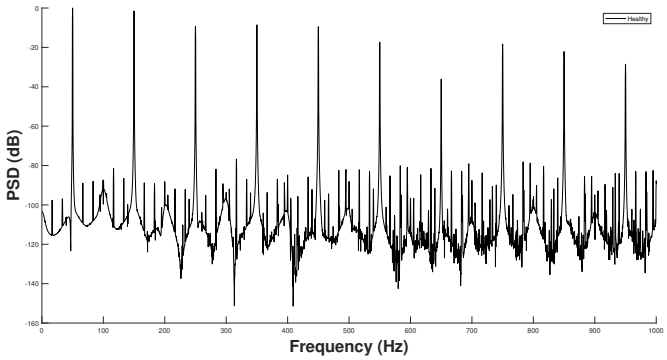

Fig. 22. Healthy case, FFT of the stray flux with full load

B. Demagnetization 50%, full load

In this subsection, the full load with healthy case is compared with uniform demagnetization, one pole demagnetization and trailing edge demagnetization which are all demagnetized by 50%.

1) Uniform demagnetization: The result of the uniform demagnetization is placed in Figure 23. All of the magnets are demagnetized by 50% which results in the blue line in the frequency spectrum provided by the fast Fourier transform. It can be seen that the uniform demagnetization causes a few changes in the amplitude when compared to the healthy case

in black. The majority of the frequency spectrum appears to have a decreased amplitude, almost like the spectrum has been ”dragged” down with bottoms marked in red. The three first bottoms have a percentage change of 9.64%, 12.7% and 11.7%. This is a very severe fault, so it is likely that some protection will notice the fault and disconnect. For the subharmonics it is present that some of the harmonics have increased and some of them decreased, but there seem to be no pattern that is repeating for the odd and even harmonics or the subharmonics.

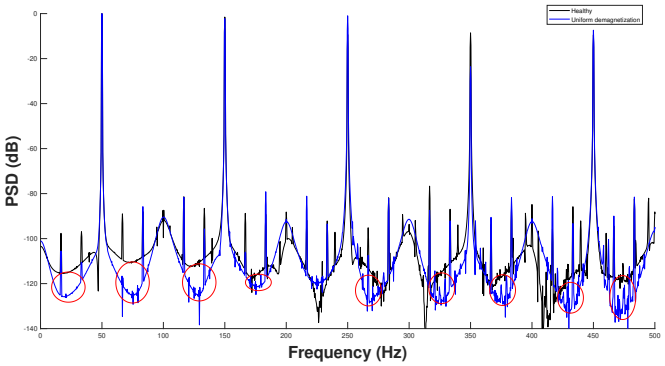

Fig. 23. Healthy (black), Uniform demagnetization (blue), full load

The comparison between a healthy magnet and a demagnetized magnet is placed in Figure 24. The healthy magnet have a value of 0.96 T and the demagnetized is 0.49 T.

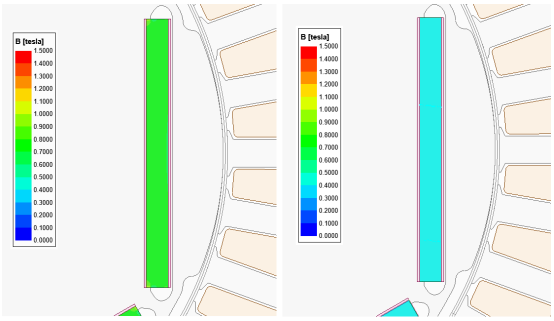

Fig. 24. Uniform demagnetization magnet comparison, healthy (left) with 0.96 T, demagnetized (right) with 0.49 T

2) One pole demagnetization: The frequency spectrum of the comparison between healthy case and one pole demagnetized by 50% is placed in Figure 25. It can be observed that an asymmetric fault has kicked in as the subharmonics $f_s(1 \pm \frac{k}{p})$ marked with red circles, where k is an index increasing (1, 2, 3), f_s is the fundamental frequency and p is pole pairs. This corresponds well with the equation 18 deduction in Chapter III-D except for the difference by P being pole pairs instead of number of poles. For example the subharmonics 16.67 Hz, 33.33 Hz, 66.67 Hz and 83.33 Hz have been increased by 73.7 dB, 83.8 dB, 78,3 dB, 73.5 dB which is a percentage change of 75.5%, 86.5%, 87.9%, 83.5%. This is a very large difference it is almost that the subharmonics have the same amount of amplitude as the odd harmonics. This fault can probably be detected without previously knowledge about the healthy case of the machine due to the large spike of these subharmonics.

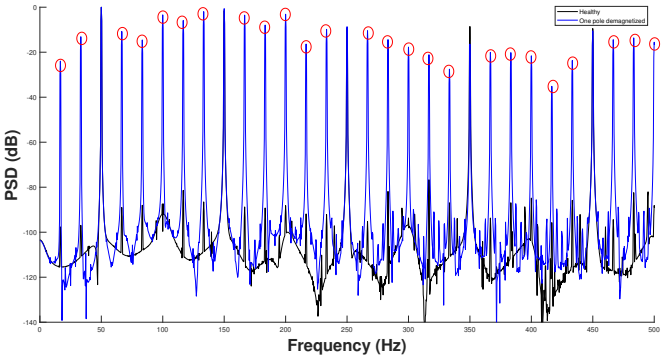

Fig. 25. Healthy (black), One pole demagnetized (blue), full load, subharmonic change marked with red circles.

3) Trailing edge demagnetization, 1/8 magnet: The healthy case and the trailing edge of 1/8 of the magnet case are very similar in terms of amplitude and structure, as illustrated in Figure 26 where the trailing edge demagnetization is applied. Further it can be observed that the subharmonics like subharmonics 16.67 Hz, 33.33 Hz, 66.67 Hz and 83.33 Hz increase with 3.4%, 14.4%, 14% and 9.6% in terms of amplitude found in Table VI in Appendix D. The odd and even harmonics are almost unchanged thus implying that the biggest change is in the amplitude of the subharmonics. However, this change is a lot less then what was observed with the one pole demagnetization, implying that it could be just noise differences.

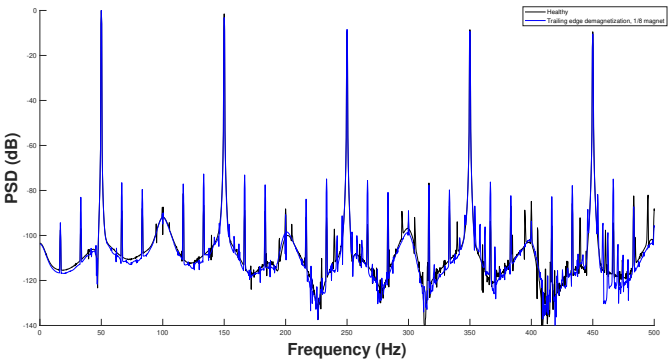

Fig. 26. Healthy (black), Trailing edge demagnetization 1/8 magnet (blue), full load

4) Trailing edge demagnetization, 1/4 magnet: The trailing edge fault with the size that cover 1/4 of the magnet with a demagnetization of 50% is placed in Figure 27. Here it is observed that there are some new subharmonics that appear in the FFT visualized with arrows pointing at them. They seems to have a pattern that follow the equation $f_s(1 \pm \frac{k}{4p})$, where k is an index increasing (1, 2, 3), f_s is the fundamental frequency and p is pole pairs as explained earlier. This means that when

a trailing edge demagnetization can be difficult to detect in the starting phase as when just 1/8 of the magnet is demagnetized on the trailing edge, but when the process has develop to a more severe fault as in Figure 27 where 1/4 of the magnet is defected, these small subharmonics appear in the FFT. It seems that the number 4 in the equation corresponds to the 1/4 of the magnet demagnetized. Although the change is small in percentage just around 2 to 7 % gathered from Table VII in Appendix D, the pattern seem to be consistent over a large span of the frequency spectrum.

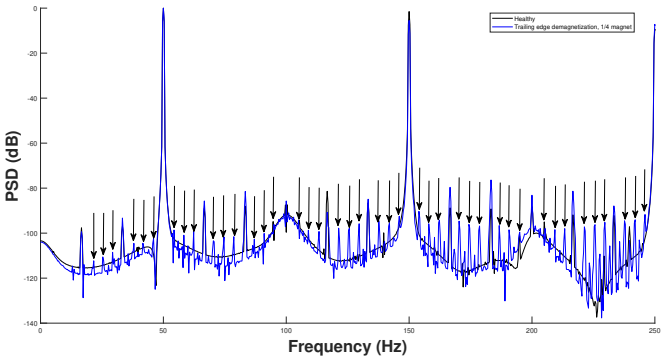

Fig. 27. Healthy (black), Trailing edge demagnetization 1/4 magnet (blue), full load, arrows marking the subharmonics change in amplitude.

In Figure 28 the magnetic field of 1/8 and 1/4 magnet trailing edge is placed. One can observe the differences between the field strength between the trailing edge of 0.49 T and the healthy part with 0.66 T of the magnet. The healthy value is lower than it was for the uniform demagnetization case even though the material specifications are the same.

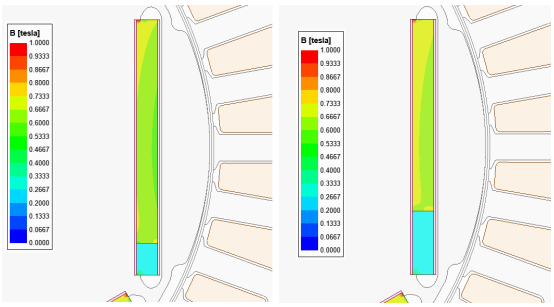

Fig. 28. Trailing edge demagnetization comparison, 1/8 magnet (left), 1/4 of the magnet (right)

The plot of the magnetic flux density of the airgap and the trailing edge of 1/4 of the magnet is seen in Figure 29. The healthy and the trailing edge scenarios almost seem the same in terms of magnetic flux density in the airgap. It can be observed that the trailing edge of the magnet contributes to a less magnetic flux in the airgap compared with the leading edge. This is due to that the stator field is align with the q-axis to gain maximum torque. The average value in airgap affected by the trailing edge part of the magnet is approximately 0.1 T compared with the leading edge part of the airgap which is around 0.5 T.

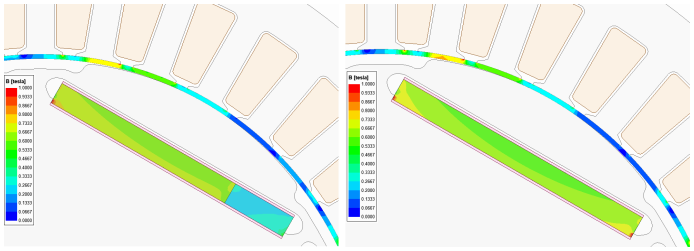

Fig. 29. Flux density of: Trailing edge of 1/4 magnet (left), Healthy (right), airgap included

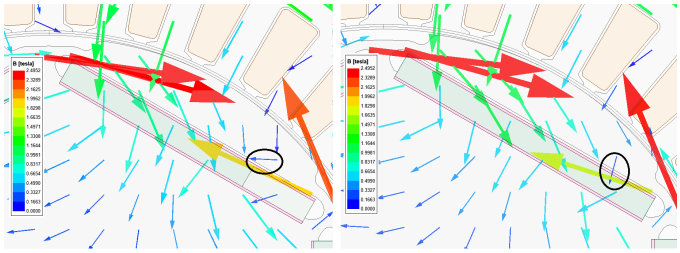

Fig. 30. Flux density vectors of: Trailing edge of 1/4 magnet (left), Healthy (right)

However, when the vector field of the magnetic flux is analyzed in Figure 30, it can be observed that the flux chooses to go through the healthy part of the magnet and ”squeezed” through that part. The vector arrow inside the black circles shows the difference, with the trailing edge scenario’s arrow changing direction to pass through the healthy part of the magnet. This is due to that the leading edge of the magnet has stronger magnetic field than the trailing edge part that is demagnetized. In the trailing edge scenario (left), it is also observed that the arrows leaving the magnet have a stronger field of around 0.75 T compared with healthy scenario of approximately 0.67 T.

5) Stray flux comparison: Figure 31 shows the waveform of the stray fluxes of the induced voltage of healthy (blue),

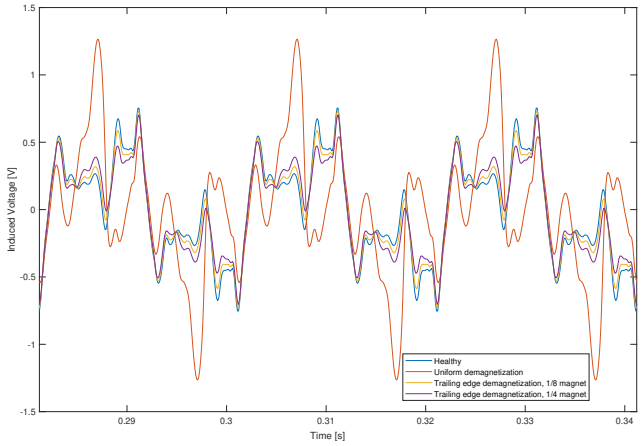

Fig. 31. Comparison of stray flux induced voltage of healthy (blue), uniform demagnetization (red), trailing edge demagnetization 1/8 magnet (yellow) and trailing edge demagnetization 1/4 magnet (purple)

uniform demagnetization (red), trailing edge demagnetization 1/8 magnet (yellow) and trailing edge demagnetization 1/4 magnet (purple) which are to be analyzed.

It can be observed that the waveform of the healthy and the trailing edge demagnetization have the same structure. Although the trailing edge waveform has a lower amplitude than the healthy with a decrease of 2.6% for 1/8 magnet and 7.1% for 1/4 magnet from the peak value. This is due to that a small part of the magnet contribute to less flux compared with healthy case. This can actually be observed outside the machine obtained by the flux sensor and can be a detection method for the trailing edge type fault. The uniform demagnetization is observed to spikes at approximately ± 1.3 V, which is an increase of 62.5 % compared with the healthy case. This can be caused by that the field from the stator is increasing to compensate for the uniform demagnetization of 50%, and therefore resulting in a larger amplitude measured by the sensor right outside the stator frame.

C. Demagnetization 50%, 50% load

In this subsection, the same analysis has been performed on a different loading condition in this subsection to compare 50% load with full load and determine whether the same results are obtained.

1) Healthy case, full load and 50% load: The healthy cases of both 50% load and full load are shown in Figure 32. The blue graph for 50% load contains some more noise than the full load. The 50% load does contain the same subharmonics as the full load which is important to be able to compare with the faults in both scenarios.

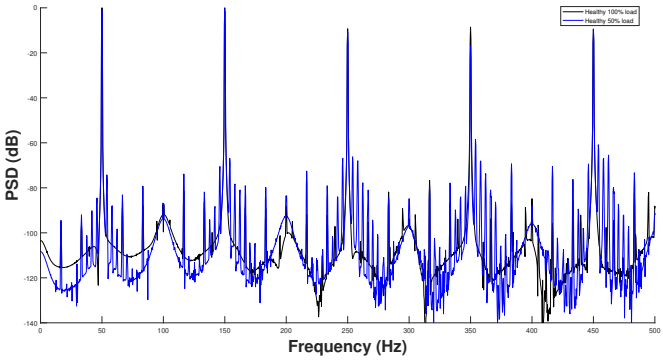

Fig. 32. Healthy case for full load (black) and 50% load (blue)

2) Uniform demagnetization: Figure 33 displays the outcome of the uniform demagnetization with 50% loading condition. In Figure 23 it was observed that the faulty spectrum was "dragged" down and these bottoms as illustrated by the ellipses drawn in the figure in red. In this scenario with 50% loading condition it seems that the frequency spectrum's match each other better. This is quite intuitive because the magnets are lowered 50% and the loading is changed 50%, thus matching each other. However, there are some minor amplitude increase for the around the area where the even harmonics marked with a purple ellipse.

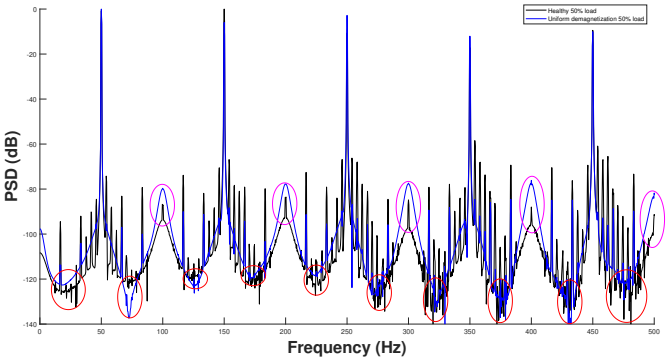

Fig. 33. Healthy (black), Uniform demagnetization (blue), 50% load

3) One pole demagnetization: The FFT of when one pole is demagnetized is placed in Figure 34. The new large harmonics is marked with red circles as previously done for the full load. This observation supports the findings in Figure 25 for the full load with one demagnetized pole because it appears to be applicable to a 50% loading condition. The subharmonics 16.67 Hz, 33.33 Hz, 66.67 Hz and 83.33 Hz have been increased by 70.5%, 81.9%, 84.7% found in Table IX in Appendix E and 81.6% which is a large difference.

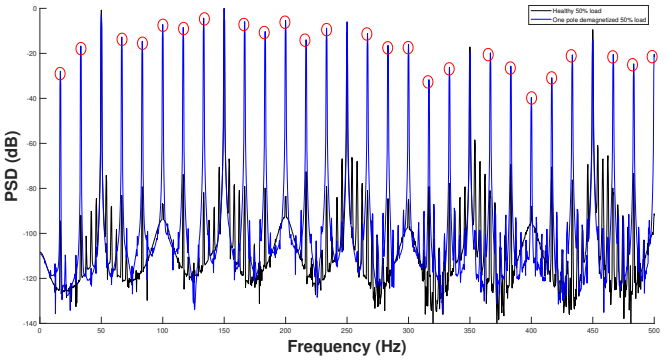

Fig. 34. Healthy (black), One pole demagnetized (blue), 50% load, subharmonic change marked with red circles.

4) Trailing edge demagnetization, 1/8 magnet: The frequency spectrum of the trailing edge demagnetization of 1/8 of the magnet with 50% loading is placed in Figure 35. It is observed that the faulty spectrum follow the healthy with some minor noise disturbances. This corresponds with the full load scenario as there is no specific or distinctive change between the healthy and faulty scenario.

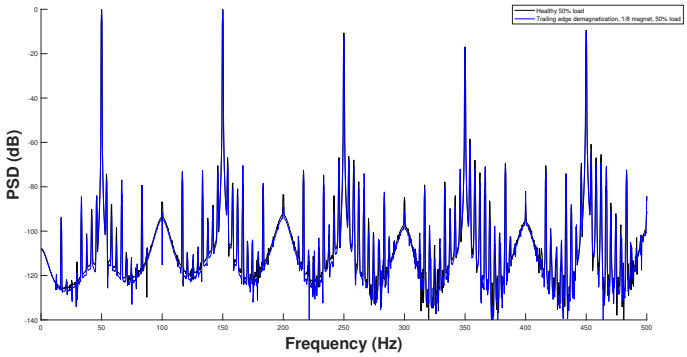

Fig. 35. Healthy (black), Trailing edge demagnetization 1/8 magnet (blue), 50% load

5) Trailing edge demagnetization, 1/4 magnet: The fault scenario where 1/4 of the magnet is demagnetized with 50% load is placed in Figure 36. It is observed that the blue graph is 2dB below the healthy along the frequency spectrum. The subharmonics that appeared earlier for the full load case does not seem to appear when the PMSM have been applied a 50% loading condition. Due to the fact that the fault is symmetrical, harmonics may be cancelled when all of the magnet's trailing edges experience a 50% demagnetization at the same time as the load is reduced to that same percentage.

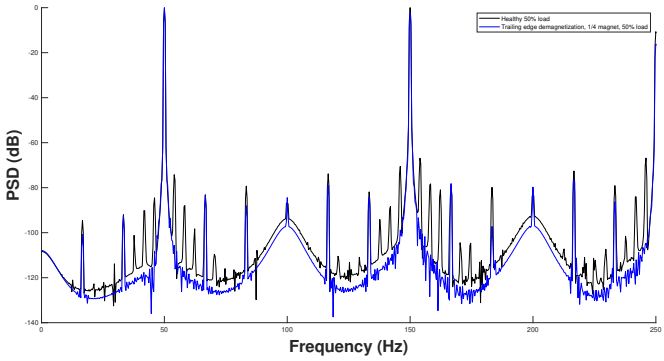

Fig. 36. Healthy (black), Trailing edge demagnetization 1/4 magnet (blue), 50% load

VIII. Future work

- Physical testes on a permanent magnet synchronous machine can be conducted to compare with the FEM results.
- AI development or software that can detect faults in the frequency spectrum by giving rules for different types of faults.
- A no-load case can be explored as there is done a 50% load in this thesis.

IX. Conclusion

In this thesis the frequency spectrum of uniform, one pole and trailing edge for both 50% load and full load in the PMSM Weg W22 are presented along with analysis of the magnetic field of different parts of the machine. The stray magnetic flux is gathered by a sensor that is mounted on top of the stator frame of the machine. A comparison between healthy and faulty case is provided to investigate the differences.

At full load with a one pole demagnetization it was found that the subharmonics following the equation $f_s(1 \pm \frac{k}{p})$ with a percentage change of 75.5%, 86.5%, 87.9% and 83.5% for the subharmonics 16.67 Hz, 33.33 Hz, 66.67 Hz and 83.33 Hz. The same pattern was observed with 50% load. The significant spike in these subharmonics suggests that this fault can be found even without prior knowledge of the machine's healthy case because they are not supposed to be so large in a healthy machine.

Trailing edge demagnetization of 1/8 of the magnet did not give any specific change in the harmonics. However, when the trailing edge was applied to 1/4 of the magnet a pattern following the equation $f_s(1 \pm \frac{k}{4p})$ appeared. This same pattern was not observable with 50% load which can be due to cancelling of the subharmonics because that the loading is changed to the same degree of demagnetization. The stray flux flux was analyzed directly and it gave a decrease of 2.6% for 1/8 magnet and 7.1% for 1/4 magnet from the peak value of healthy case.

For uniform demagnetization at full load the majority of the frequency spectrum appears to have a decreased amplitude with these bottoms that are marked. However, for the 50% load case the FFT's of the healthy and faulty case seem to match each other better which can be because both magnets and the loading is reduced 50%. The uniform demagnetization is distinguished from healthy case when it is analyzed and compared with the stray flux induced voltage where spikes with an increase of 62.5% compared with the healthy case. This can be caused by that the field from the stator is increased to compensate for the uniform demagnetization of 50%.

To summarize it seems that the FFT can detect the one pole demagnetization fault and the trailing edge demagnetization of 1/4 of the magnet. By looking at the stray flux directly it appears that one can detect the uniform demagnetization and both the trailing edge demagnetization scenarios.

X. Acknowledgements

I would like to express gratitude to my supervisor, Professor Arne Nysveen for precious assistance and inspirational meetings. To Hossein Ehya for guiding regarding the simulation and model. To my friends and family for supporting me along the semester.

References

[1] S. B. Lee et al., "Condition Monitoring of Industrial Electric Machines: State of the Art and Future Challenges," in IEEE Industrial Electronics Magazine, vol. 14, no. 4, pp. 158-167, Dec. 2020, doi: 10.1109/MIE.2020.3016138.

[2] N. Haraguchi, C. F. C. Cheng, and E. Smeets, "The importance of manufacturing in economic development: Has this changed?," World Develop., vol. 93, pp. 293–315, 2017.

[3] V. Gurusamy, G. -A. Capolino, B. Akin, H. Henao, R. Romary and R. Pusca, "Recent Trends in Magnetic Sensors and Flux-Based Condition Monitoring of Electromagnetic Devices," in IEEE Transactions on Industry Applications, vol. 58, no. 4, pp. 4668-4684, July-Aug. 2022, doi: 10.1109/TIA.2022.3174804.

[4] Pindoriya, Rajesh. (2020). Comparative Review of Brushless PMAC and PMDC Motor Drives. 10.36227/techrxiv.12951515.

[5] Levkin, Dmitry, 2023, "Permanent magnet synchronous motor" https: //en.engineering-solutions.ru/motorcontrol/pmsm/

[6] J. R. Riba, A. Garcia, and L. Romeral, "Demagnetization diagnosis in permanent magnet synchronous motors under non-stationary speed conditions," Electr. Power Syst. Res., vol. 80, no. 10, pp. 1277–1285, Oct. 2010.

[7] A. Khlaief, M. Boussak and M. Gossa, "Open phase faults detection in PMSM drives based on current signature analysis," The XIX International Conference on Electrical Machines - ICEM 2010, Rome, Italy, 2010, pp. 1-6, doi: 10.1109/ICELMACH.2010.5607977.

[8] Ehya, H., Nysveen, A., Nilssen, R. and Liu, Y. (2021), Static and dynamic eccentricity fault diagnosis of large salient pole synchronous generators by means of external magnetic field. IET Electr. Power Appl, 15: 890-902. https://doi.org/10.1049/elp2.12068

[9] Mazaheri-Tehrani, E., Faiz, J.: Airgap and stray magnetic flux monitoring techniques for fault diagnosis of electrical machines: an overview. IET Electr. Power Appl. 16(3), 277– 299 (2022). https://doi.org/10.1049/elp2.12157

[10] Riitala, A.: Estimating the speed of a permanent magnet synchronous machine using magnetic leakage flux. Ph.D. thesis, Lappeenranta University of Technology (2018)

[11] Keysan, O.: A non-invasive speed and position sensor for induction machines using external search coils. Ph.D. thesis, Middle East Technical University (2009)

[12] The Business Research Company (2022) "Global Permanent Magnet Synchronous Motor (PMSM) Market". Available at https://www.thebusinessresearchcompany.com/report/ permanent-magnet-synchronous-motor-global-market-report

[13] S.B.Ringdal. Fault Detection in Permanent Magnet Machines Utilized in e-aviation and Wind Applications. Project report in TET4510, Department of Electric Energy, NTNU – Norwegian University of Science and Technology, Dec. 2022 unpublished: Trondheim (exact replication)

[14] S.B.Ringdal. Fault Detection in Permanent Magnet Machines Utilized in e-aviation and Wind Applications. Project report in TET4510, Department of Electric Energy, NTNU – Norwegian University of Science and Technology, Dec. 2022 unpublished: Trondheim (additional information or 'modification')

[15] Department of Information Security and Communication Technology (02.12.2020). Reusing text from the project in your master thesis. Accessed 02.02.23 at https://innsida.ntnu.no/wiki/-/wiki/English/Reuse+of+text.

[16] G.W.C. Kaye T.H. Laby, Table of Physical and Chemical Constants, 14th ed, Longman

[17] I. Sadeghi, H. Ehya and J. Faiz, "Eccentricity fault indices in large induction motors an overview," 2017 8th Power Electronics, Drive Systems Technologies Conference (PEDSTC), Mashhad, Iran, 2017, pp. 329-334, doi: 10.1109/PEDSTC.2017.7910347.

[18] J. Farooq, S. Srairi, A. Djerdir, and A. Miraoui, "Use of permeance network method in the demagnetization phenomenon modelling in a permanent magnet," IEEE Trans. Magn., vol. 42, no. 4, pp. 1295–1298, Apr. 2006.

[19] J.R. Hendershot, T.J.E. Miller, Design of brushless permanent magnet motors, Motor Design Books LLC, Munich, Germany, 2010.

[20] J. Hong et al., "Detection and classification of rotor demagnetization and eccentricity faults for PM synchronous motors," IEEE Trans. Ind. Appl., vol. 48, no. 3, pp. 923-932, May/June 2012.

[21] "Three-phase power representations: abc frame, frame and dq frame" YouTube, uploaded by Prof. Pedro Almeida, 15.02.17, https://www. youtube.com/watch?v=vdeVVTltr1M&ab_channel=Prof.PedroAlmeida

[22] W. C. Duesterhoeft; Max W. Schulz; Edith Clarke (July 1951). "Determination of Instantaneous Currents and Voltages by Means of Alpha, Beta, and Zero Components". Transactions of the American Institute of Electrical Engineers. 70 (2): 1248–1255. doi:10.1109/T-AIEE.1951.5060554. ISSN 0096-3860. S2CID 51636360.

[23] F. Tahri, A.Tahri, Eid A. AlRadadi and A. Draou Senior, "Analysis and Control of Advanced Static VAR compensator Based on the Theory of the Instantaneous Reactive Power," presented at ACEMP, Bodrum, Turkey, 2007.

[24] R.H. Park Two Reaction Theory of Synchronous Machines AIEE Transactions 48:716–730 (1929).

[25] K.-C. Kim, S.-B. Lim, D.-H. Koo, and J. Lee, "The shape design of permanent magnet for permanent magnet synchronous motor," IEEE Trans. Magn., vol. 42, no. 10, pp. 3485–3487, Oct. 2006.

[26] J. Farooq, S. Srairi, A. Djerdir, and A. Miraoui, "Use of permeance network method in the demagnetization phenomenon modelling in a permanent magnet," IEEE Trans. Magn., vol. 42, no. 4, pp. 1295–1298, Apr. 2006.

[27] Anne Marie Helmenstine (2019): "How to Demagnetize a Magnet" https://www. thoughtco.com/how-to-demagnetize-a-magnet-607873

[28] S. Yu and R. Tang, "Electromagnetic and mechanical characterization of noise and vibration in permanent magnet synchronous machines," IEEE Trans. Magn., vol. 42, no. 4, pp. 1335–1338, Apr. 2006.

[29] Klyve, Ø. S., "Magnetic Modelling of Saturated IPMSMs, for Improved Torque Estimation and Accurate MTPA Control," Master thesis, Department of Electric Power Energineering, Norwegian University of Science and Technology (NTNU), Trondheim, Norway, 2021.

[30] W. Le Roux, R. G. Harley and T. G. Habetler, "Detecting rotor faults in permanent magnet synchronous machines," 4th IEEE International Symposium on Diagnostics for Electric Machines, Power Electronics and Drives, 2003. SDEMPED 2003., Atlanta, GA,USA, 2003, pp. 198-203, doi: 10.1109/DEMPED.2003.1234573.

[31] H. Kim, J. Hur, "Dynamic characteristic analysis of irreversible demagnetization in SPM- and IPM-type BLDC motors," IEEE Trans. Ind. Appl., vol. 53, no. 2, pp. 982-990, March/April 2017.

[32] Electrical Engineering, Harmonics in Synchronous Machines(Alternators) — Slot Harmonics. Available at https://www.electricalengineeringinfo.com/2016/12/ harmonics-slot-harmonicsin-synchronous-machines-alternators.html

[33] J. Jeong, H. Lee, M. O. Zapico, S. B. Lee, D. D. Reigosa and F. B. del Blanco, "Trailing Edge PM Demagnetization in Surface PM Synchronous Motors: Analysis and Detection," 2022 IEEE Energy Conversion Congress and Exposition (ECCE), Detroit, MI, USA, 2022, pp. 1-7, doi: 10.1109/ECCE50734.2022.9948151.

[34] J. -C. Urresty, J. -R. Riba, M. Delgado and L. Romeral, "Detection of Demagnetization Faults in Surface-Mounted Permanent Magnet Synchronous Motors by Means of the Zero-Sequence Voltage Component," in IEEE Transactions on Energy Conversion, vol. 27, no. 1, pp. 42-51, March 2012, doi: 10.1109/TEC.2011.2176127.

[35] J. Zhao, L. Wang, L. Xu, F. Dong, J. Song and X. Yang, "Uniform Demagnetization Diagnosis for Permanent-Magnet Synchronous Linear Motor Using a Sliding-Mode Velocity Controller and an ALN-MRAS Flux Observer," in IEEE Transactions on Industrial Electronics, vol. 69, no. 1, pp. 890-899, Jan. 2022, doi: 10.1109/TIE.2021.3050360.

[36] V. Gurusamy, G. -A. Capolino, B. Akin, H. Henao, R. Romary and R. Pusca, "Recent Trends in Magnetic Sensors and Flux-Based Condition Monitoring of Electromagnetic Devices," in IEEE Transactions on Industry Applications, vol. 58, no. 4, pp. 4668-4684, July-Aug. 2022, doi: 10.1109/TIA.2022.3174804.

[37] Mazaheri-Tehrani, E., Faiz, J.: Airgap and stray magnetic flux monitoring techniques for fault diagnosis of electrical machines: an overview. IET Electr. Power Appl. 16(3), 277– 299 (2022). https://doi.org/10.1049/elp2.12157

[38] Frosini, L., Harlisca, C., Szabo, L.: Induction machine bearing fault detection by means of statistical processing of the stray flux measurement. IEEE Trans. Ind. Electron. 62(3), 1846–1854 (2015)

[39] I. Zamudio-Ramirez, R. A. Osornio-Rios, J. A. Antonino-Daviu, H. Razik and R. d. J. Romero-Troncoso, "Magnetic Flux Analysis for the Condition Monitoring of Electric Machines: A Review," in IEEE Transactions on Industrial Informatics, vol. 18, no. 5, pp. 2895-2908, May 2022, doi: 10.1109/TII.2021.3070581.

[40] Y. Park et al., "Stray flux monitoring for reliable detection of rotor faults under the influence of rotor axial air ducts," IEEE Trans. Ind. Electron., vol. 66, no. 10, pp. 7561–7570, Oct. 2019.

[41] H. Ehya, A. Nysveen and J. A. Antonino-Daviu, "Advanced Fault Detection of Synchronous Generators Using Stray Magnetic Field," in IEEE Transactions on Industrial Electronics, vol. 69, no. 11, pp. 11675-11685, Nov. 2022, doi: 10.1109/TIE.2021.3118363.

[42] J. -R. Riba Ruiz, J. A. Rosero, A. Garcia Espinosa and L. Romeral, "Detection of Demagnetization Faults in Permanent-Magnet Synchronous Motors Under Nonstationary Conditions," in IEEE Transactions on

Magnetics, vol. 45, no. 7, pp. 2961-2969, July 2009, doi: 10.1109/T-MAG.2009.2015942.
[43] J. G. Proakis and D. K. Manolakis, Digital Signal Processing (4th Edition), 4th ed. Prentice Hall, 2006.
[44] Heideman, Michael T.; Johnson, Don H.; Burrus, Charles Sidney (1984). "Gauss and the history of the fast Fourier transform" (PDF). IEEE ASSP Magazine. 1 (4): 14–21. CiteSeerX 10.1.1.309.181. doi:10.1109/MASSP.1984.1162257. S2CID 10032502. Archived (PDF) from the original on 2013-03-19.
[45] Van Loan, Charles (1992). Computational Frameworks for the Fast Fourier Transform. SIAM.
[46] H. Bai, "A three order harmonic injection method to reduce current harmonics for high speed PM generator," The 2nd International Symposium on Power Electronics for Distributed Generation Systems, 2010, pp. 631-634, doi: 10.1109/PEDG.2010.5545833.
[47] P. P. Jadhav and A. S. Patil, "Reduce harmonics using PI controller in d-q reference frame for active power filter," 2016 International Conference on Global Trends in Signal Processing, Information Computing and Communication (ICGTSPICC), 2016, pp. 653-656, doi: 10.1109/ICGTSPICC.2016.7955382.
[48] Kothari, D.P. and Nagrath, I.J. (2010). Electric Machines, 5th edition. New Delhi: Tata McGrw Hill
[49] B. M. Ebrahimi and J. Faiz, "Feature extraction for short-circuit fault detection in permanent-magnet synchronous motors using stator-current monitoring," IEEE Trans. Power Electron., vol. 25, no. 10, pp. 2673–2682, Oct. 2010.
[50] B. G. Gu, J. H. Choi, and I. S. Jung, "Development and analysis of interturn short fault model of PMSMs with series and parallel winding connections," IEEE Trans. Power Electron., vol. 29, no. 4, pp. 2016–2026, Apr. 2014.
[51] https://www.electronics-tutorials.ws/accircuits/harmonics.html
[52] Gandhi, A.; Corrigan, T.; Parsa, L. Recent Advances in Modeling and Online Detection of Stator Interturn Faults in Electrical Motors. IEEE Trans. Ind. Electron. 2011, 58, 1564–1575.
[53] Y. Qi, E. Bostanci, V. Gurusamy and B. Akin, "A Comprehensive Analysis of Short-Circuit Current Behavior in PMSM Interturn Short-Circuit Faults," in IEEE Transactions on Power Electronics, vol. 33, no. 12, pp. 10784-10793, Dec. 2018, doi: 10.1109/TPEL.2018.2809668.
[54] J. Hang, S. Ding, J. Zhang, M. Cheng, W. Chen and Q. Wang, "Detection of Interturn Short-Circuit Fault for PMSM With Simple Fault Indicator," in IEEE Transactions on Energy Conversion, vol. 31, no. 4, pp. 1697-1699, Dec. 2016, doi: 10.1109/TEC.2016.2583780.
[55] G.-H. Kang, J. Hur, H. Nam, J.-P. Hong, and G.-T. Kim, "Analysis of irreversible magnet demagnetization in line-start motors based on the finite-element method," IEEE Trans. Magn., vol. 39, no. 3, pp. 1488–1491, May 2003.
[56] Ehya, H., Nysveen, A., Nilssen, R. and Liu, Y. (2021), Static and dynamic eccentricity fault diagnosis of large salient pole synchronous generators by means of external magnetic field. IET Electr. Power Appl, 15: 890-902. https://doi.org/10.1049/elp2.12068
[57] H. Wang, S. Liu, S. Wu, L. Guo and T. Shi, "Optimal Design of Permanent Magnet Structure to Reduce Unbalanced Magnetic Pull in Surface-Mounted Permanent-Magnet Motors," in IEEE Access, vol. 8, pp. 77811-77819, 2020, doi: 10.1109/ACCESS.2020.2989803.
[58] Gieras, Jacek F. Permanent magnet motor technology : design and applications / Jacek F. Gieras. – 3rd ed. p. cm. Includes bibliographical references and index. ISBN 978-1-4200-6440-7 (hardcover : alk. paper) 1. Permanent magnet motors. I. Title.
[59] J. -C. Urresty, R. Atashkhooei, J. -R. Riba, L. Romeral and S. Royo, "Shaft Trajectory Analysis in a Partially Demagnetized Permanent-Magnet Synchronous Motor," in IEEE Transactions on Industrial Electronics, vol. 60, no. 8, pp. 3454-3461, Aug. 2013, doi: 10.1109/TIE.2012.2213565.
[60] D. Casadei, F. Filippetti, C. Rossi, and A. Stefani, "Magnets faults characterization for permanent magnet synchronous motors," in Proc. 7th IEEE Int. Symp. Power Electron. Drives Diagnostics Electr. Mach. (SDEMPED), Cargese, France, 2009, pp. 1–6.
[61] S. Rajagopalan, "Detection of rotor and load faults in brushless dc motors operating under stationary and nonstationary conditions," Ph.D. Thesis, Georgia Institute of Technology, Atlanta, GA, Aug. 2006.
[62] Nicola Bianchi. Electrical machine analysis using finite elements. CRC press, 2005.
[63] Winding layout, Emetor, 2023 https://www.emetor.com/glossary/winding-layout/

APPENDIX

A. WINDING LAYOUT

The single layer three phase winding layout showing the phases with upper-case letters A, B, C for the conductors in one direction and lower-case for the return conductors [63].

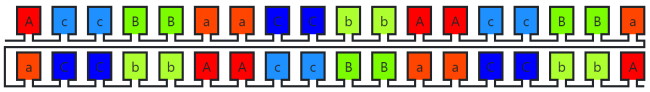

Fig. 37. Winding layout, showing the single layer setup for the PMSM

B. DQ-THETA ALIGNMENT TORQUE

The torque used for the voltage alignment in the q-axis.

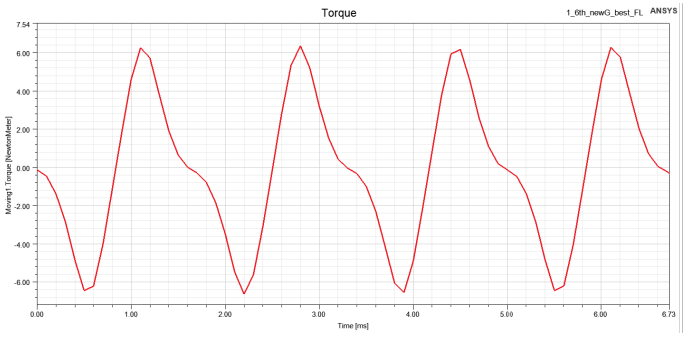

Fig. 38. Torque in zero current condition

C. DESIGN DATA OF THE MOTOR

The design for the PMSM in Ansys based on the design in [29].

TABLE III
MOTOR DATA

Name	Description	Value	Unit
Ls	Axial length stator	80.8	mm
Dso	Outer stator diameter	210	mm
Dsi	Inner stator diameter	150	mm
Dri	Inner rotor diameter	47.5	mm
Dro	Outer rotor diameter	147.5	mm
airgap	Air gap	1.25	mm
Oa	Outer air diameter	240	mm
hPM	Height PM	5	mm
wPM	Width PM	60	mm
hs	Slot height stator	20	mm
Thh	Tooth head height	1.5	mm
Tws	Tooth width stem	6.2	mm
Twh	Tooth width head	10	mm
slots	Slots/teeths	36	
mag_slot_lower	Lower part of mag slot	Dri/2 + 32	mm
mag_slot_height	Magnet slot height	6	mm
D_slot_circ	Circle in magnet slot	4.5	mm

D. FFT TABLES, FULL LOAD

The FFT tables for full load with specific frequency harmonics with its corresponding amplitude value. Healthy and faulty scenario are compared and the percentage difference is calculated.

TABLE IV
ONE POLE DEMAGNETIZATION, FULL LOAD

Harmonic frequency [Hz]	Healthy [dB]	Faulty [db]	Difference [%]
16,67	-97,64	-23,92	75,50
33,33	-96,93	-13,12	86,47
50,00	0,00	0,00	0,00
66,66	-89,00	-10,78	87,88
83,33	-88,01	-14,55	83,46
100,00	-99,60	-3,41	96,57
116,66	-81,41	-5,92	92,73
133,33	-86,53	-1,96	97,73
150,00	-1,52	-0,65	57,40
166,66	-88,77	-3,52	96,03
183,33	-89,23	-7,94	91,10
199,99	-88,18	-3,12	96,46
216,66	-91,87	-16,37	82,18
233,33	-92,15	-9,83	89,33
249,99	-9,32	-8,68	6,88
266,66	-95,18	-10,45	89,02
283,32	-81,86	-14,41	82,39
299,99	-93,67	-17,72	81,08
316,66	-76,68	-21,13	72,45
333,32	-86,94	-27,54	68,32
349,99	-8,57	-16,39	-91,30
366,65	-93,70	-20,05	78,60
383,32	-86,90	-20,19	76,77
399,99	-84,83	-21,62	74,52
416,65	-95,72	-35,15	63,28
433,32	-85,82	-23,69	72,39
449,99	-9,49	-10,50	-10,73
466,65	-94,40	-14,44	84,70
483,32	-82,42	-13,64	83,45
499,98	-88,13	-15,57	82,34

TABLE V
UNIFORM DEMAGNETIZATION, FULL LOAD

Harmonic frequency [Hz]	Healthy [dB]	Faulty [db]	Difference [%]
16,67	-97,64	-105,53	-8,08
33,33	-96,93	-110,64	-14,15
50,00	0,00	0,00	0,00
66,66	-89,00	-134,66	-51,30
83,33	-88,01	-85,78	2,53
100,00	-99,60	-90,31	9,33
116,66	-81,41	-81,59	-0,22
133,33	-86,53	-95,70	-10,59
150,00	-1,52	-2,23	-46,65
166,66	-88,77	-105,97	-19,37
183,33	-89,23	-79,17	11,27
199,99	-88,18	-91,43	-3,69
216,66	-91,87	-81,14	11,68
233,33	-92,15	-93,49	-1,45
249,99	-9,32	-0,98	89,48
266,66	-95,18	-107,42	-12,86
283,32	-81,86	-82,00	-0,17
299,99	-93,67	-91,35	2,47
316,66	-76,68	-87,41	-13,99
333,32	-86,94	-92,07	-5,90
349,99	-8,57	-23,62	-175,74
366,65	-93,70	-90,54	3,37
383,32	-86,90	-81,80	5,87
399,99	-84,83	-91,12	-7,41
416,65	-95,72	-81,35	15,01
433,32	-85,82	-93,29	-8,70
449,99	-9,49	-7,37	22,31
466,65	-94,40	-89,97	4,69
483,32	-82,42	-81,51	1,10
499,98	-88,13	-94,98	-7,77

TABLE VI
TRAILING EDGE 1/8 MAGNET, FULL LOAD

Harmonic frequency [Hz]	Healthy [dB]	Faulty [db]	Difference [%]
16,67	-97,64	-94,33	3,38
33,33	-96,93	-83,02	14,35
50,00	0,00	0,00	0,00
66,66	-89,00	-76,53	14,01
83,33	-88,01	-79,54	9,62
100,00	-99,60	-94,93	4,69
116,66	-81,41	-77,09	5,30
133,33	-86,53	-72,66	16,04
150,00	-1,52	-3,20	-110,35
166,66	-88,77	-73,10	17,65
183,33	-89,23	-77,49	13,15
199,99	-88,18	-90,78	-2,95
216,66	-91,87	-83,85	8,73
233,33	-92,15	-74,87	18,76
249,99	-9,32	-8,42	9,59
266,66	-95,18	-75,58	20,59
283,32	-81,86	-80,83	1,25
299,99	-93,67	-89,01	4,98
316,66	-76,68	-77,69	-1,31
333,32	-86,94	-79,75	8,27
349,99	-8,57	-9,28	-8,32
366,65	-93,70	-76,22	18,65
383,32	-86,90	-82,33	5,26
399,99	-84,83	-93,58	-10,32
416,65	-95,72	-82,76	13,54
433,32	-85,82	-77,84	9,30
449,99	-9,49	-10,44	-10,10
466,65	-94,40	-74,90	20,65
483,32	-82,42	-87,27	-5,89
499,98	-88,13	-95,63	-8,50

TABLE VII
TRAILING EDGE 1/4 MAGNET, FULL LOAD

Harmonic frequency [Hz]	Healthy [dB]	Faulty [db]	Difference [%]
16,67	-97,64	-99,39	-1,80
21,67	-115,33	-112,30	2,62
25,33	-114,33	-110,56	3,30
29,33	-112,35	-108,51	3,42
33,33	-96,93	-93,29	3,75
38,00	-108,37	-104,55	3,53
41,67	-106,56	-104,47	1,96
46,00	-109,54	-102,42	6,50
50,00	0,00	0,00	0,00
54,33	-102,55	-98,61	3,84
58,33	-105,39	-100,92	4,24
62,33	-107,50	-99,30	7,62
66,66	-89,00	-85,70	3,72
70,66	-110,43	-103,82	5,98
74,66	-110,54	-101,68	8,02
78,66	-109,69	-101,58	7,40
83,33	-88,01	-81,48	7,42
87,00	-106,71	-102,70	3,75
91,00	-104,12	-100,15	3,82
95,00	-103,28	-96,17	6,88
100,00	-99,60	-85,71	13,95
105,00	-96,22	-94,24	2,05
109,00	-102,67	-98,74	3,82
113,33	-107,63	-99,26	7,77
116,66	-81,41	-90,76	-11,48
121,33	-112,22	-97,79	12,86
125,66	-112,49	-97,89	12,98
129,66	-109,43	-95,83	12,43
133,33	-86,53	-84,92	1,87
137,66	-106,53	-94,44	11,34
142,00	-103,65	-95,40	7,96
146,00	-96,86	-92,50	4,50
150,00	-1,52	-5,50	-261,83
153,99	-100,52	-90,31	10,16
157,99	-105,53	-95,84	9,19
161,99	-109,61	-95,41	12,96
166,66	-88,77	-79,63	10,29
170,33	-116,93	-94,66	19,04
174,33	-118,59	-96,12	18,95
178,66	-115,01	-96,81	15,83
183,33	-89,23	-76,38	14,40
186,66	-112,16	-96,64	13,83
190,66	-113,25	-98,53	13,00
194,99	-101,25	-99,52	1,71
205,33	-99,84	-97,96	1,88
199,99	-88,18	-83,15	5,71
207,33	-104,26	-102,24	1,94
209,33	-106,34	-98,47	7,40
213,33	-110,56	-98,00	11,36
216,66	-91,87	-81,35	11,45
221,33	-120,96	-97,21	19,64
223,33	-124,26	-113,24	8,87
225,66	-130,37	-96,23	26,19
227,66	-130,55	-109,32	16,26
231,66	-121,74	-105,68	13,19
229,66	-122,28	-95,22	22,13
233,33	-92,15	-87,90	4,61
235,66	-116,21	-103,77	10,70
237,66	-114,07	-94,51	17,15
239,66	-97,16	-103,26	-6,27
241,99	-110,34	-94,06	14,76
243,66	-108,03	-103,03	4,63
245,99	-102,22	-91,72	10,27
249,99	-9,32	-7,22	22,55

E. FFT TABLES, 50% LOAD

The FFT tables for 50% load with specific frequency harmonics with its corresponding amplitude value. Healthy and faulty scenario are compared and the percentage difference is calculated.

TABLE VIII
HEALTHY FULL LOAD AND HEALTHY 50% LOAD COMPARISON

Harmonic frequency [Hz]	Healthy full load [dB]	Healthy 50% load [dB]	Difference [%]
16,67	-97,64	-94,48	3,24
33,33	-96,93	-92,02	5,06
50,00	0,00	-0,79	0,00
66,66	-89,00	-83,14	6,58
83,33	-88,01	-79,30	9,90
100,00	-99,60	-87,25	12,40
116,66	-81,41	-73,85	9,29
133,33	-86,53	-81,87	5,39
150,00	-1,52	0,00	100,00
166,66	-88,77	-79,09	10,90
183,33	-89,23	-79,84	10,52
199,99	-88,18	-83,79	4,98
216,66	-91,87	-72,59	20,99
233,33	-92,15	-79,10	14,17
249,99	-9,32	-10,68	-14,64
266,66	-95,18	-80,99	14,91
283,32	-81,86	-84,54	-3,27
299,99	-93,67	-84,82	9,44
316,66	-76,68	-79,18	-3,25
333,32	-86,94	-77,85	10,46
349,99	-8,57	-17,16	-100,36
366,65	-93,70	-84,09	10,26
383,32	-86,90	-69,34	20,20
399,99	-84,83	-87,97	-3,71
416,65	-95,72	-70,47	26,38
433,32	-85,82	-76,25	11,15
449,99	-9,49	-9,46	0,28
466,65	-94,40	-82,50	12,60
483,32	-82,42	-73,33	11,02
499,98	-88,13	-91,30	-3,60

TABLE IX
ONE POLE DEMAGNETIZATION, 50% LOAD

Harmonic frequency [Hz]	Healthy [dB]	Faulty [db]	Difference [%]
16,67	-94,48	-27,92	70,45
33,33	-92,02	-16,70	81,85
50,00	-0,79	-2,86	-261,23
66,66	-83,14	-12,71	84,71
83,33	-79,30	-14,62	81,56
100,00	-87,25	-7,19	91,76
116,66	-73,85	-8,52	88,47
133,33	-81,87	-4,33	94,72
150,00	0,00	0,00	0,00
166,66	-79,09	-5,90	92,54
183,33	-79,84	-10,29	87,11
199,99	-83,79	-5,31	93,66
216,66	-72,59	-13,95	80,79
233,33	-79,10	-8,76	88,92
249,99	-10,68	-5,97	44,12
266,66	-80,99	-11,22	86,14
283,32	-84,54	-16,42	80,57
299,99	-84,82	-15,97	81,18
316,66	-79,18	-31,67	60,00
333,32	-77,85	-26,18	66,37
349,99	-17,16	-19,31	-12,51
366,65	-84,09	-19,77	76,48
383,32	-69,34	-25,68	62,96
399,99	-87,97	-39,54	55,05
416,65	-70,47	-30,83	56,26
433,32	-76,25	-20,67	72,89
449,99	-9,46	-13,97	-47,69
466,65	-82,50	-20,45	75,22
483,32	-73,33	-24,65	66,38
499,98	-91,30	-20,41	77,64

TABLE X
UNIFORM DEMAGNETIZATION, 50% LOAD

Harmonic frequency [Hz]	Healthy [dB]	Faulty [db]	Difference [%]
16,67	-94,48	-114,08	-20,75
33,33	-92,02	-104,13	-13,16
50,00	0,00	0,00	0,00
66,66	-83,14	-96,98	-16,64
83,33	-79,30	-99,97	-26,07
100,00	-87,25	-79,65	8,72
116,66	-73,85	-90,05	-21,94
133,33	-81,87	-91,22	-11,42
150,00	0,00	-5,98	0,00
166,66	-79,09	-94,25	-19,16
183,33	-79,84	-103,25	-29,33
199,99	-83,79	-77,78	7,17
216,66	-72,59	-91,30	-25,78
233,33	-79,10	-95,49	-20,73
249,99	-10,68	-2,81	73,73
266,66	-80,99	-95,82	-18,32
283,32	-84,54	-95,84	-13,38
299,99	-84,82	-77,35	8,81
316,66	-79,18	-89,34	-12,84
333,32	-77,85	-88,13	-13,21
349,99	-17,16	-12,05	29,82
366,65	-84,09	-85,96	-2,23
383,32	-69,34	-84,55	-21,93
399,99	-87,97	-76,16	13,43
416,65	-70,47	-84,93	-20,51
433,32	-76,25	-84,84	-11,27
449,99	-9,46	-10,08	-6,51
466,65	-82,50	-88,66	-7,47
483,32	-73,33	-89,75	-22,39
499,98	-91,30	-81,76	10,46

TABLE XI
TRAILING EDGE 1/8 MAGNET, 50% LOAD

Harmonic frequency [Hz]	Healthy [dB]	Faulty [db]	Difference [%]
16,67	-94,48	-93,67	0,86
33,33	-92,02	-84,47	8,21
50,00	0,00	0,00	0,00
66,66	-83,14	-76,90	7,51
83,33	-79,30	-79,51	-0,27
100,00	-87,25	-115,24	-32,08
116,66	-73,85	-73,06	1,06
133,33	-81,87	-72,65	11,26
150,00	0,00	0,00	0,00
166,66	-79,09	-70,44	10,95
183,33	-79,84	-78,45	1,74
199,99	-83,79	-90,27	-7,73
216,66	-72,59	-72,92	-0,46
233,33	-79,10	-74,73	5,52
249,99	-10,68	-12,52	-17,24
266,66	-80,99	-74,06	8,56
283,32	-84,54	-82,38	2,55
299,99	-84,82	-90,54	-6,74
316,66	-79,18	-80,94	-2,22
333,32	-77,85	-80,66	-3,62
349,99	-17,16	-16,91	1,46
366,65	-84,09	-70,91	15,67
383,32	-69,34	-69,55	-0,30
399,99	-87,97	-82,16	6,60
416,65	-70,47	-72,06	-2,25
433,32	-76,25	-74,03	2,91
449,99	-9,46	-10,28	-8,68
466,65	-82,50	-70,79	14,20
483,32	-73,33	-72,42	1,25
499,98	-91,30	-84,32	7,64

TABLE XII
TRAILING EDGE 1/4 MAGNET, 50% LOAD

Harmonic frequency [Hz]	Healthy [dB]	Faulty [db]	Difference [%]
16,67	-94,48	-100,79	-6,69
21,67	-128,50	-129,09	-0,46
25,33	-122,16	-128,52	-5,21
29,33	-132,54	-127,03	4,16
33,33	-92,02	-92,65	-0,69
38,00	-108,55	-120,05	-10,60
41,67	-90,19	-117,67	-30,48
46,00	-84,52	-108,19	-28,00
50,00	-0,79	0,00	100,00
54,33	-76,79	-116,14	-51,24
58,33	-87,96	-120,06	-36,50
62,33	-98,30	-120,65	-22,74
66,66	-83,14	-83,53	-0,46
70,66	-110,56	-126,44	-14,37
74,66	-115,96	-126,23	-8,86
78,66	-126,00	-124,61	1,10
83,33	-79,30	-88,03	-11,01
87,00	-111,41	-116,33	-4,41
91,00	-107,54	-110,19	-2,47
95,00	-99,34	-102,77	-3,46
100,00	-87,25	-84,43	3,23
105,00	-98,81	-103,03	-4,28
109,00	-107,23	-110,87	-3,39
113,33	-115,66	-117,92	-1,95
116,66	-73,85	-78,82	-6,73
121,33	-117,30	-125,75	-7,20
125,66	-121,90	-125,92	-3,30
129,66	-114,65	-123,01	-7,30
133,33	-81,87	-84,11	-2,73
137,66	-94,13	-116,90	-24,18
142,00	-88,30	-111,26	-26,01
146,00	-70,54	-98,81	-40,08
150,00	0,00	0,00	0,00
153,99	-66,90	-102,85	-53,74
157,99	-78,84	-128,37	-62,82
161,99	-84,14	-116,37	-38,30
166,66	-79,09	-78,19	1,14
170,33	-104,46	-124,03	-18,73
174,33	-105,71	-131,54	-24,44
178,66	-131,11	-125,40	4,36
183,33	-79,84	-97,23	-21,79
186,66	-110,60	-117,21	-5,97
190,66	-105,75	-110,29	-4,29
194,99	-98,41	-102,41	-4,06
205,33	-99,39	-103,55	-4,19
199,99	-83,79	-79,76	4,81
207,33	-102,46	-107,55	-4,97
209,33	-107,65	-111,42	-3,50
213,33	-111,19	-118,28	-6,38
216,66	-72,59	-76,47	-5,35
221,33	-120,53	-126,15	-4,66
223,33	-122,15	-128,05	-4,83
225,66	-116,30	-125,56	-7,96
227,66	-120,13	-128,49	-6,97
231,66	-118,63	-125,02	-5,39
229,66	-107,37	-130,80	-21,82
233,33	-79,10	-86,25	-9,04
235,66	-113,19	-126,40	-11,66
237,66	-101,55	-117,19	-15,40
239,66	-112,49	-115,80	-2,94
241,99	-84,10	-112,07	-33,26
243,66	-107,96	-109,94	-1,84
245,99	-66,85	-104,70	-56,62
249,99	-10,68	-16,11	-50,82

F. The MATLAB codes

The MATLAB codes used for different calculations and plots explained by their heading.

A. BH-curve of magnet

```
plot([-763944 0], [0 0.96], LineWidth
    =1)
ylabel('B [T]');
xlabel('H [AT/m]');
ylim([0,1.1])
xlim([-900000,0])

hold on

plot([-390000 0], [0 0.49], LineWidth
    =1)
ylabel('B [T]');
xlabel('H [AT/m]');
ylim([0,1.1])
xlim([-900000,0])
```

B. FFT plots to table values

```
fig = openfig('
    healthy_vs_one_pole_demag_50.fig');
fig = gcf;
axObjs = fig.Children;
dataObjs = axObjs.Children;
x = dataObjs(2).XData;
y = dataObjs(2).YData;

x1 = [];
y1 = [];
i = 51;

for u = 1:30
x1(u,1) = x(1,i);
y1(u,1) = y(1,i);
i = i + 50;
end

%x1 = [];
%y1 = [];
%i = 51;
%v = [51;66;77;89;101;115;
% 126;139;151;164;176;188;
% 201;213;225;237;251;262;
% 274;286;301;316;328;341;
% 351;365;378;390;401;414;
% 427;439;451;463;475;487;
% 501;512;524;537;551;561;
% 573;586;617;601;623;629;
% 641;651;665;671;678;684;
% 696;690;701;708;714;720;
% 727;732;739;751];
%for u = 1:66
%x1(u,1) = x(1,v(u));
%y1(u,1) = y(1,v(u));
%i = i + 50;
%end
```

C. FFT in chapter V-B

```
f=100; %frequency of sine wave
overSampRate=30; %oversampling rate
fs=overSampRate*f; %sampling frequency
phase =0; %desired phase shift in
    radians
nCyl = 1; %to generate five cycles of
    sine wave

t=0:1/fs:nCyl*1/f; %time base

x=cos(2*pi*f*t+phase); %replace with
    cos if a cosine wave is desired
plot(t,x);
title(['Sine Wave f=', num2str(f), 'Hz
    ']);
xlabel('Time(s)');
ylabel('Amplitude');


NFFT=1024;
X=fftshift(fft(x,NFFT));
fVals=fs*(-NFFT/2:NFFT/2-1)/NFFT;
plot(fVals,abs(X),'b');
%title('Double Sided FFT - with
    FFTShift');
xlabel('Frequency (Hz)')
ylabel('|DFT Values|');
```

D. Graph plots of stray flux, torque, radial/tangent airgap flux, BH-curve of steel

```
filename = 'torque_50.csv';
A = readmatrix(filename);

tid = A(:,1);
spenning = A(:,2);


width = 3;

plot(tid,spenning)

hold on
```

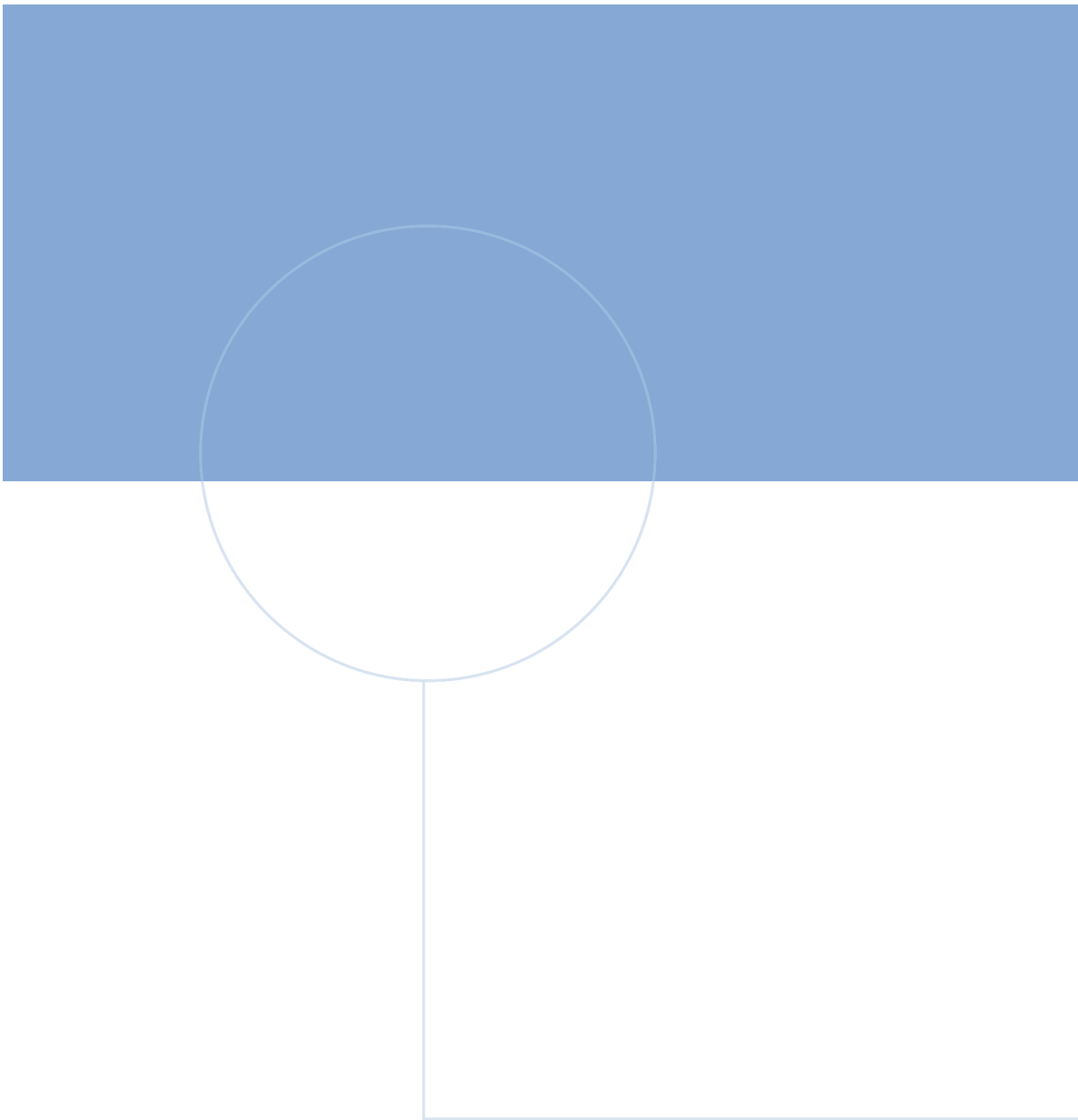

NTNU

Norwegian University of
Science and Technology